

Transparent-to-Dark Electrochromic Behavior in Naphthalene-Diimide-Based Mesoporous MOF-74 Analogs

By

Khalid Al Kaabi  
B.Sc. Chemical Engineering  
Cornell University, 2014

Submitted to the Department of Chemistry in Partial Fulfillment of the Requirements for the Degree of Master of Science in Chemistry

at the

Massachusetts Institute of Technology

September 2016

© 2016 Massachusetts Institute of Technology. All rights reserved.

  
Signature redacted

Signature of Author: \_\_\_\_\_

Department of Chemistry  
July 26<sup>th</sup>, 2016

  
Signature redacted

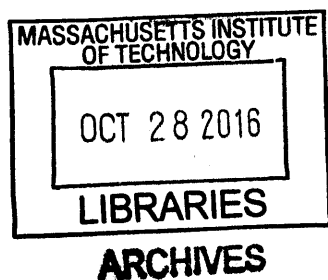
Certified by: \_\_\_\_\_

Mircea Dincă  
Associate Professor of Chemistry  
Thesis Supervisor

  
Signature redacted

Accepted by: \_\_\_\_\_

Robert W. Field  
Haslam and Dewey Professor of Chemistry  
Chairman, Departmental Committee on Graduate Students



Transparent-to-Dark Electrochromic Behavior in Naphthalene-Diimide-Based Mesoporous  
MOF-74 Analogs

By

Khalid Al Kaabi  
B.Sc. Chemical Engineering  
Cornell University, 2014

Submitted to the Department of Chemistry on August 6th, 2016 in Partial Fulfillment of the  
Requirements for the Degree of Master of Science in Inorganic Chemistry  
at the Massachusetts Institute of Technology

**ABSTRACT**

The deliberate insertion of redox-active naphthalene diimide ligands in the versatile family of metal-organic frameworks known as MOF-74 (CPO-27) gives rise to a mesoporous electrochromic MOF that can be switched from transparent to dark, a desirable feature in electrochromic devices such as smart windows. Specifically, we report two new materials with the MOF-74 topology that display redox activity stemming from a naphthalene diimide salicylic acid (NDISA) ligand. We show that the new materials can be deposited as thin films on fluorine-doped tin oxide glass. The surprisingly different morphology of MOF films obtained from  $Mg^{2+}$  and  $Ni^{2+}$  ions is likely controlled by the nucleation kinetics of  $Mg_2(NDISA)$  and  $Ni_2(NDISA)$ , respectively. Both materials exhibit well-behaved quasi-reversible redox events associated with the  $[NDI]/[NDI]^-$  and  $[NDI]^-/[NDI]^{2-}$  redox couples, which are also responsible for the electrochromic switching.

Thesis supervisor: Mircea Dincă  
Title: Associate Professor of Chemistry

## **To My Loving Mother and Father.**

Khalid Al Kaabi obtained his B.Sc. degree in Chemical Engineering (*magna cum laude*) from Cornell University in 2014. During his time at Cornell he developed interest in theoretical chemistry and decided to pursue research with Prof. Roald Hoffmann. His work with Prof. Hoffmann was a very inspiring experience and resulted in the publication of two papers in the Journal of American Chemical Society entitled “*Ionic N-B-N- and B-N-B-substituted benzene analogues: a theoretical analysis,*” and “*Silicon Monoxide at 1 atm and Elevated Pressures: Crystalline or Amorphous?*” As a result, Khalid decided to pursue a graduate degree in chemistry at MIT, and joined Prof. Mircea Dincă’s lab where he worked on designing redox-active MOFs for electrochromic applications. His work with Prof. Dincă appeared on the cover of the new high-impact journal Chem (Cell Press) entitled “*Transparent-to-Dark Electrochromic Behavior in Naphthalene-Diimide-Based Mesoporous MOF-74 Analogs.*” After two years at MIT, Khalid decided to complete his M.Sc. degree in chemistry.

<b>Abstract</b>	2
<b>Dedication</b>	3
<b>Table of Contents</b>	4
<b>List of Tables and Figures</b>	5

## **Table of Contents**

<b>1. Background and Introduction</b>	6
a. Electrochromism: definition, materials, and applications.	6
b. Metal-organic frameworks as a new class of electrochromic materials.	8
c. Introduction of ligand-based redox-activity in MOF-74 (CPO-27).	9
d. References.	10
<b>2. Electrochromic Behavior in Naphthalene-Diimide-Based Mesoporous MOF-74 Analogs</b>	12
a. Introduction.	12
b. Synthesis and structural characterization.	13
c. Thin film deposition.	15
d. Electrochemical and spectroelectrochemical studies.	17
e. Discussion and Summary.	20
f. Experimental procedures and supplementary information.	21
g. Author contributions and acknowledgements.	39
h. References and notes.	40
<b>3. Appendix A. Structural Information: CIF Files for Simulated Structures.</b>	42
a. Mg-NDISA CIF file.	42
b. Ni-NDISA CIF file.	48
<b>Curriculum Vitae</b>	54

## List of Tables and Figures

<b>Figure 1.1.</b> A schematic representation of a typical electrochromic device.	6
<b>Figure 1.2.</b> Structure of MOF-74 built with 2,5-dioxidoterephthalate (DOT) as the organic linker. The SBU forms 1D chains of $M_2O_2(CO_2)_2$ clusters.	9
<b>Figure 2.1.</b> Synthesis and simulated structure of <b>M-NDISA</b> viewed along the c axis. A representation of the secondary building unit is shown. Teal, blue, red, and grey spheres represent metal (Mg or Ni), N, O, and C atoms, respectively. H atoms are omitted for clarity.	15
<b>Figure 2.2.</b> Scanning electron micrographs of (a,b) <b>Ni-NDISA</b> (at 400 nm and 200 nm magnifications, respectively) and (c,d) <b>Mg-NDISA</b> (at 4 $\mu\text{m}$ and 2 $\mu\text{m}$ magnifications, respectively) thin films. (e) Simulated and experimental PXRD patterns of <b>Mg-NDISA</b> and <b>Ni-NDISA</b> powders and thin-films (peaks labeled with * correspond to FTO).	16
<b>Table 2.1.</b> Redox potentials for <b>Mg-NDISA</b> , <b>Ni-NDISA</b> , and $H_4NDISA$ .	17
<b>Figure 2.3.</b> Spectroelectrochemical data of <b>Ni-NDISA</b> collected by transmission UV/Vis spectroscopy showing the reversible formation of $[NDI]^-$ and $[NDI]^{2-}$ when (a) $-0.5\text{ V} \rightarrow -2\text{ V}$ reducing and (b) $-2\text{ V} \rightarrow -0.5\text{ V}$ oxidizing step-potentials are applied (vs. $Fc/Fc^+$ ). (c) Images of reversible color switching of <b>Ni-NDISA</b> films at several reducing potentials ( $-1.6\text{ V}$ , $-2\text{ V}$ , and $-2.3\text{ V}$ vs. $Fc/Fc^+$ ). Complete reversibility to the neutral transparent state is achieved by applying a reverse anodic bias ( $-0.7\text{ V}$ vs. $Fc/Fc^+$ ). All measurements were performed in 0.1 M $[(^n\text{Bu})_4\text{N}]\text{PF}_6/\text{DMF}$ solution using a three-electrode setup, and the UV/Vis spectra were collected at 1 second intervals (see Experimental Procedures for details).	19
<b>Scheme S1.</b> Synthesis of $H_4NDISA$ .	27
<b>Table S1.</b> Summary of cell parameters and Pawley refinement details for <b>M-NDISA</b> .	27
<b>Figure S1.</b> Simulated, experimental, and Pawley refined PXRD patterns of <b>M-NDISA</b> .	28
<b>Figure S2.</b> Thin films of <b>Mg-NDISA</b> and <b>Ni-NDISA</b> deposited on FTO slides.	29
<b>Figure S3.</b> Cyclic voltammograms of <b>Ni-NDISA</b> and <b>Mg-NDISA</b> .	30
<b>Figure S4.</b> Cyclic voltammogram of $H_4NDISA$ .	31
<b>Figure S5.</b> PXRD of <b>Mg-NDISA</b> before and after electrochemical cycling.	32
<b>Figure S6.</b> PXRD of <b>Ni-NDISA</b> before and after electrochemical cycling.	33
<b>Figure S7.</b> UV/Vis absorbance spectrum and spectroelectrochemistry of <b>Mg-NDISA</b> .	34
<b>Figure S8.</b> UV/Vis absorbance spectra of <b>Ni-NDISA</b> and $H_4NDISA$ .	35
<b>Figure S9.</b> $N_2$ adsorption isotherm of <b>Ni-NDISA</b> .	36
<b>Figure S10.</b> $^1\text{H}$ NMR of $H_4NDISA$ .	37
<b>Figure S11.</b> $^{13}\text{C}$ NMR of $H_4NDISA$ .	38

## 1. Background and Introduction.

### a. Electrochromism: definition, materials, and applications.

Electrochromism is defined as the reversible optical switching between two or more states caused by electron-transfer processes or by the application of electric potential.<sup>1</sup> Recently, electrochromic materials have gained extensive interest due to their potential utility in energy saving applications such as smart windows and displays.<sup>1,2b-c</sup> In addition to cost, there are several metrics that need to be simultaneously optimized for incorporation of electrochromic materials in commercial devices. These metrics include switching time, coloration and write-erase efficiencies, life cycle, and processability.<sup>1</sup> A typical electrochromic device is constructed from two transparent electrodes, ion conductor, ion storage film, and electrochromic film (Figure 1.1).<sup>2c</sup> Applying electric potential between the two electrodes polarizes the electrochromic film(s), which results in flow of counter ions from the ion storage film into the electrochromic material, resulting in changes to the optical properties of the film.

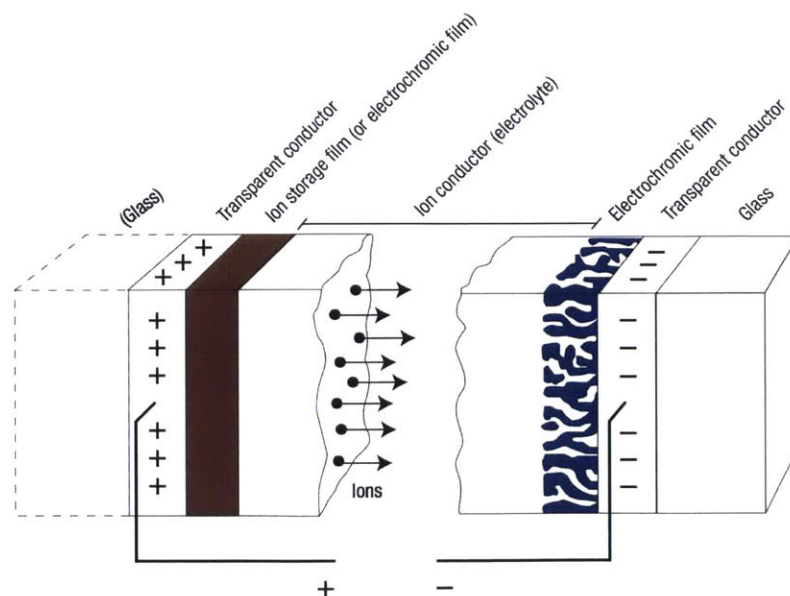


**Figure 1.1:** A schematic representation of a typical electrochromic device.<sup>2c</sup> Reproduced with permission from Nature Publishing Group ©.

In most cases, the coloration mechanism (and therefore the switching time) is governed by how fast counter ions can intercalate the material or how fast electrons flow (i.e. hop) through the film. Transition-metal oxides (e.g.  $\text{WO}_3$ ) are among the first materials to be investigated for their electrochromic properties and are currently being used in commercial smart windows.<sup>1</sup> The partial reduction of W(VI) centers to W(V) results in color switching from pale yellow to intense blue. However, this color switching usually suffers from long switching times, and low coloration efficiencies (partly limited by the extent to which W(VI) centers can be reduced without resulting in irreversible behavior). Therefore, recent efforts have been directed towards designing organic and organic-inorganic hybrid electrochromes as alternative materials for electrochromic devices.<sup>2,3</sup> Generally, organic based electrochromic materials exhibit faster switching times and excellent coloration efficiencies (i.e. more intense coloration per charge inject into the material) but usually suffer from photochemical instability (especially when exposed to UV light).<sup>1,2b</sup> A recent successful example of organic based electrochromic materials was reported by Reynolds et al.<sup>3</sup> where donor-acceptor organic based polymers were utilized to achieve transparent-to-black switching. These electrochromic polymers were synthesized by polymerizing oligomers constructed from 3,4-bis(2-ethylhexyloxy)thiophene as electron donor units and 2,1,3-benzothiadiazole as acceptors. By varying the ratio of donors to acceptors, several polymers with different resting colors were synthesized. This approach was utilized to obtain a material that exhibit optical absorption over the entire visible spectrum (i.e. black) which can be switched to transparent by oxidizing the material with electrical anodic bias of less than 1 V. Despite the recent success of organic-based compounds for the design of electrochromic materials, there is still need for the discovery of new materials with improved and tunable properties.

## **b. Metal-organic frameworks as a new class of electrochromic materials.**

Metal-organic frameworks (MOFs) have emerged as new class of materials with variety of promising application such as catalysis,<sup>4</sup> gas storage,<sup>5</sup> and separation.<sup>6</sup> Because of their high porosities as well as structural and compositional tunability, MOFs are potential candidates for electrochromic applications.<sup>7</sup> The large pores in MOFs are beneficial for electrolyte transport,<sup>8</sup> and therefore could result in fast switching times and efficient write-erase behavior, while the compositional variability between the organic linker and the metal centers provide tunable parameters for the optical behavior in these materials. Since the optical properties in MOFs can be tuned by varying both the metal center and the organic ligand, this provides additional degree of tunability not available in either organic-based or inorganic-based materials. The first example of electrochromic behavior in MOFs was reported by Dincă et al.<sup>7a</sup> where three different water-stable, pyrazolate-based naphthalene diimide (NDI) MOFs were synthesized. These MOFs were easily deposited on fluorine-doped tin oxide (FTO) substrate directly from solutions of the ligands and  $\text{Zn}(\text{NO}_3)_2 \cdot 6\text{H}_2\text{O}$  at 130 °C forming films of  $\text{Zn}(\text{NDI-X})$ . The resting color of these films was tuned by functionalizing the organic ligand with appropriate functional groups ( $\text{Zn}(\text{NDI-X})$  where  $X = \text{H}$  (pale yellow),  $\text{NHEt}$  (blue), and  $\text{SEt}$  (orange)). Cyclic voltammetry measurements displayed well-behaved, quasi-reversible redox processes associated with the reduction and subsequent re-oxidation of the MOFs. Optical images as well as UV/Vis measurement indicated that the MOFs exhibit reversible electrochromic behavior as a result of the redox behavior of the organic ligand. The coloration efficiency (CE) of these MOFs exceeded  $100 \text{ cm}^2\text{C}^{-1}$  in the blue region of the spectrum; these CE values are higher than common inorganic electrochromic materials and comparable to conductive organic polymers. Another example of electrochromism in MOFs was reported by Hupp et al.<sup>7d</sup> where the synthesis



and thin film deposition of NU-901, a redox-active MOF, on FTO was demonstrated. NU-901 thin films can be switched from a yellow neutral state to a blue oxidized state by the application of anodic bias that results in the oxidation of the ligand. The films show fast switching ( $\sim 6-10$  s) and excellent coloration efficiency ( $204 \text{ cm}^2\text{C}^{-1}$  at 587 nm). Despite the precedence in the literature, there is still a need to investigate electrochromic MOFs with new topologies and improved physical properties. That is, synthesizing electrochromic MOFs with new and well-defined topologies would provide a platform to fundamentally understand the structure-function relationship in the context of electrochromism.

### c. Introduction of ligand-based redox-activity in MOF-74 (CPO-27)

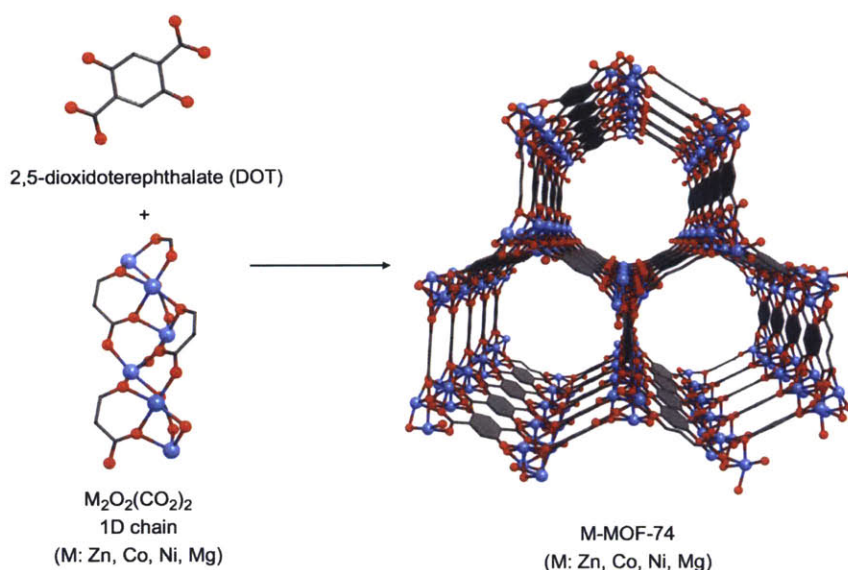


**Figure 1.2:** Structure of MOF-74 built with 2,5-dioxidoterephthalate (DOT) as the organic linker. The SBU forms 1D chains of  $M_2O_2(CO_2)_2$  clusters.<sup>9c</sup> Reproduced with permission from Elsevier ©.

Structures with the MOF-74 (CPO-27) topology represent a unique class of materials that have found variety of utilities, and have arguably driven the advancement of the entire field with their applications ranging from gas storage to catalysis.<sup>9</sup> MOF-74 type structures crystallize in hexagonal space groups (typically  $R\bar{3}$  or  $R\bar{3}c$ ), and form one-dimensional metal chains

( $M_2O_2(CO_2)_2$  clusters) as their secondary-building units (SBUs) (Figure 1.2). Although members of the MOF-74 family can show ligand-based redox activity<sup>9d</sup>, this is usually associated with the oxidation of the phenol group that ligates metal centers, and, therefore, compromises the structural integrity of the framework. We envisioned that designing MOF-74 analogs with ligand-based redox activity that avoids the above mentioned problem would be attractive not only from an applied point of view but also for fundamental studies of redox-active MOFs. MOF-74 type structures represent an interesting class of materials because of (1) the ability to isoreticularly expand pore size without inducing structural collapse or interpenetration, (2) the ability to obtain isostructural forms with variety of metals, (3) a high degree of thermal and chemical stability relative to many other MOFs, and (4) the availability of unsaturated metal centers with open coordination sites. Therefore, the introduction of ligand-based redox activity in MOF-74 type structures could represent a starting point for the development of variety of derivatives that take advantage of the unique properties found in this class of materials. Our strategy for designing new redox-active and electrochromic MOF-74 type structures relied on the incorporation of naphthalene diimide ligands into the framework. The results of this quest are described in Chapter 2.

## References

---

<sup>1</sup> Monk, P. M. S.; Mortimer, R. J.; Rosseinsky, D. R. *Electrochromism and Electrochromic Devices*. Cambridge University Press: New York, 2007.

<sup>2</sup> a) Hsu, P. -C.; Wang, S.; Narasimhan, V. K.; Kong, D.; Lee, H. R.; Cui, Y. (2013) Performance enhancement of metal nanowire transparent conducting electrodes by mesoscale metal wires. *Nat. Commun.* 4, 2522. b) Somani, Prakash R.; Radhakrishnan, S. Electrochromic materials and devices: present and future. *Materials Chemistry and Physics*. **2003**, 77, 117–133. c) Granqvist, C. G. (2006) Electrochromic materials: out of a niche. *Nat. Mater.* 5, 89-90.

<sup>3</sup> Beaujuge, P. M.; Ellinger, S.; Reynolds, J. R. (2008) The donor-acceptor approach allows a black-to-transmissive switching polymeric electrochrome. *Nat. Mater.* 7, 795.

<sup>4</sup> a) Kornienko, N.; Zhao, Y.; Kley, C. S.; Zhu, C.; Kim, D.; Lin, S.; Chang, C. J.; Yaghi, O. M.; Yang, P. (2015) Metal–organic frameworks for electrocatalytic reduction of carbon dioxide *J.*

---

*Am. Chem. Soc.* 137, 14129–14135. b) Ahrenholtz, S. R.; Epley, C. C.; Morris, A. J. (2014) Solvothermal preparation of an electrocatalytic metalloporphyrin MOF thin film and its redox hopping charge-transfer mechanism. *J. Am. Chem. Soc.* 136 (6), 2464–2472. c) Metzger, E. D.; Brozek, C. K.; Comito, R. J.; Dincă, M. (2016) Selective dimerization of ethylene to 1-Butene with a porous catalyst. *ACS Cent. Sci.*, 2 (3), 148–153.

<sup>5</sup> Murray, L. J.; Dincă, M.; Long, J. R. (2009) Hydrogen storage in metal-organic frameworks. *Chem. Soc. Rev.*, 38, 1294–1314.

<sup>6</sup> Cadiou, A.; Adil, K.; Bhatt, P. M.; Belmabkhout, Y.; Eddaoudi, M. (2016) A metal-organic framework-based splitter for separating propylene from propane. *Science*, 353, 6295, 137–140.

<sup>7</sup> a) Wade, C. R.; Li, M.; Dincă, M. (2013) Facile deposition of multicolored electrochromic metal-organic framework thin films. *Angew. Chem., Int. Ed.* 52 (50), 13377–13381. b) Garai, B.; Mallick, A.; Banerjee, R. (2016) Photochromic metal-organic frameworks for inkless and erasable printing. *Chem. Sci.* 7, 2195–2200. c) Usov, P. M.; Fabian, C.; D'Alessandro, D. M. (2012) Rapid determination of the optical and redox properties of a metal-organic framework *via in situ* solid state spectroelectrochemistry. *Chem. Comm.* 48(33), 3945–3. d) Kung, C. W.; Wang, T. C.; Mondloch, J. E.; Fairen-Jimenez, D.; Gardner, D. M.; Bury, W.; Klingsporn, J. M.; Barnes, J. C.; Van Duyne, R.; Stoddart, J. F.; Wasielewski, M. R.; Farha, O. K.; Hupp, J. T. (2013) Metal-organic framework thin films composed of free-standing acicular nanorods exhibiting reversible electrochromism. *Chem. Mater.* 25, 5012–5017. e) D'Alessandro, D. (2016) Exploiting redox activity in metal-organic frameworks: concepts, trends and perspectives *Chem. Commun.* 52, 8957 – 8971.

<sup>8</sup> Aubrey, M. L.; Ameloot, R.; Wiers, B. M.; Long, J. R. (2014) Metal-organic frameworks as solid magnesium electrolytes. *Energy Environ. Sci.*, 7, 667.

<sup>9</sup> a) Deng, H.; Grunder, S.; Cordova, K. E.; Valente, C.; Furukawa, H.; Hmadeh, M.; Gandara, F.; Whalley, A. C.; Liu, Z.; Asahina, S.; Kazumori, H.; O'Keeffe, M.; Terasaki, O.; Stoddart, J. F.; Yaghi, O. M. (2012) Large-pore apertures in a series of metal-organic frameworks. *Science* 336, 1018. b) Kapelewski, M. T.; Geier, S. J.; Hudson, M. R.; Stück, D.; Mason, J. A.; Nelson, J. N.; Xiao, D. J.; Hulvey, Z.; Gilmour, E.; FitzGerald, S. A.; Head-Gordon, M.; Brown, C. M.; Long, J. R. (2014) M<sub>2</sub>(m-dobdc) (M = Mg, Mn, Fe, Co, Ni) metal-organic frameworks exhibiting increased charge density and enhanced H<sub>2</sub> binding at the open metal sites. *J. Am. Chem. Soc.* 136(34), 12119–12129. c) Cozzolino, A. F.; Brozek, C. K.; Palmer, R. D.; Yano, J.; Li, M.; Dincă, M. (2014) Ligand redox non-innocence in the stoichiometric oxidation of Mn 2(2,5-dioxidoterephthalate) (Mn-MOF-74). *J. Am. Chem. Soc.* 136(9), 3334 –3337. d) Aubrey, M. L.; Long, J. R. (2015) A dual-ion battery cathode via oxidative insertion of anions in a metal-organic framework. *J. Am. Chem. Soc.* 137, 13594–13602. e) Grant Glover, T.; Peterson, G. W.; Schindler, B. J.; Britt, D.; Yaghi, O. (2011) MOF-74 building unit has a direct impact on toxic gas adsorption. *Chem. Eng. Sci.* 66, 163.

## 2. Electrochromic Behavior in Naphthalene-Diimide-Based Mesoporous MOF-74 Analogs

*Khalid AlKaabi, Casey R. Wade, and Mircea Dincă\**

This chapter was published as an article in the chemistry journal *Chem* (Cell Press) under

DOI: 10.1016/j.chempr.2016.06.013

### a. Introduction

Tuning the electronic structure of metal–organic frameworks (MOFs) by incorporating redox-active components is a powerful strategy for expanding the functionality of this class of compounds. This approach can give rise to materials with enhanced performance in applications such as electrocatalysis,<sup>1</sup> photo- and electrochromism,<sup>2</sup> and devices made from conductive MOFs.<sup>3</sup> Although MOFs offer a high degree of structural and compositional tunability, which makes them attractive for the design of optoelectronic devices, their implementation in such devices is partly limited by the inherent difficulty associated with their processing.<sup>3,4</sup> Indeed, most MOFs are obtained as insoluble microcrystalline powders,<sup>5</sup> and the development of processing methods, such as thin film deposition, must be pursued in congruence with the development of new physical properties, such as electrochromism.<sup>6</sup> Here, we demonstrate that naphthalene diimide (NDI), a redox-active molecule whose optical properties change with the redox state, can be substituted with salicylic acid groups to yield MOFs with the same topology as the well-known MOF-74.<sup>7</sup> This class of materials can be expanded isoreticularly without pore collapse, and here too we observe a pore size reaching the mesoporous regime, which is beneficial for electrolyte transport in the context of electrochromism. Although MOFs in the MOF-74 family can show ligand-based redox activity, this is usually associated with the oxidation of the phenol group that ligates the secondary building unit; this oxidation weakens the M-O bond and can compromise structural integrity.<sup>7c,d</sup> Here, we show that use of the NDI ligand

leads to well-defined reversible redox couples that are also responsible for fast transparent-to-dark optical switching, a desirable feature in electrochromic devices.

Owing to their electron deficient and aromatic nature, as well as their facile functionalization, NDIs have been extensively investigated as *n*-type semiconductors in organic electronics.<sup>8</sup> Because functionalization of the NDI core leads to derivatives that can absorb the full visible spectrum,<sup>8a</sup> these molecules have been employed in MOF-based applications that target optical reading of an input or analyte, such as sensing,<sup>9</sup> and electro- or photo-chromism.<sup>2</sup> However, many NDI-based MOFs feature topologies that are prone to interpenetration and/or exhibit metal-dependent polymorphism. When optical output is important, this is problematic because the absorption and emission spectra can be influenced by excitonic coupling processes due to the relative proximity of NDI cores. Furthermore, interpenetration generally reduces pore aperture and can impede electrolyte transport in electrochromic applications. We surmised that incorporating NDI-based linkers in mesoporous materials with the MOF-74 topology would provide solutions for both of these challenges while allowing for reversible redox activity in an otherwise robust set of materials.

## **b. Synthesis and characterization**

Condensation of 5-amino-2-hydroxybenzoic acid with 1,4,5,8-naphthalenetetracarboxylic dianhydride in *N,N*-dimethylformamide (DMF) produced *N,N'*-bis(3-carboxy-4-hydroxyphenyl)-1,4,5,8-naphthalenetetracarboximide (NDI-bis-salicylate, H<sub>4</sub>NDISA) in 70% yield (Scheme S1). Subsequent reaction of H<sub>4</sub>NDISA with Mg(NO<sub>3</sub>)<sub>2</sub>·6H<sub>2</sub>O or Ni(NO<sub>3</sub>)<sub>2</sub>·6H<sub>2</sub>O in a mixture of DMF, ethanol, and water at 120 °C for 1 day resulted in the precipitation of [Mg<sub>2</sub>(NDISA)(H<sub>2</sub>O)<sub>2</sub>]<sub>2</sub>·4(H<sub>2</sub>O) (**Mg-NDISA**) or [Ni<sub>2</sub>(NDISA)(H<sub>2</sub>O)<sub>2</sub>]<sub>2</sub>·4(H<sub>2</sub>O) (**Ni-NDISA**) as dark orange or brown microcrystalline powders, respectively. Powder X-ray diffraction (PXRD)

patterns of materials dried using supercritical CO<sub>2</sub> matched those simulated from model structures predicted based on the known MOF-74 topology (Figures 2.1 and 2.2). Pawley refinement for both materials was performed against the experimental PXRD patterns ( $R_{wp} = 5.90\% - 7.98\%$ . See Figure S1 and Table S1), and it was found that the MOFs crystallize in trigonal space groups with lattice parameters  $a = b \sim 59 \text{ \AA}$ .<sup>10</sup> The  $c$  parameter was not refined due to the low observed intensity of high-angle peaks; however, we do not expect it to deviate significantly from the values reported in other frameworks with the MOF-74 topology (i.e.  $c \sim 6.5 \text{ \AA}$ ).<sup>7</sup> As expected, the structures exhibit one-dimensional channels with pore diameter of approximately 3.3 nm (no solvent molecules were included in the model). Importantly, these mesopores should facilitate ion/electrolyte transport during electrochromic cycling.

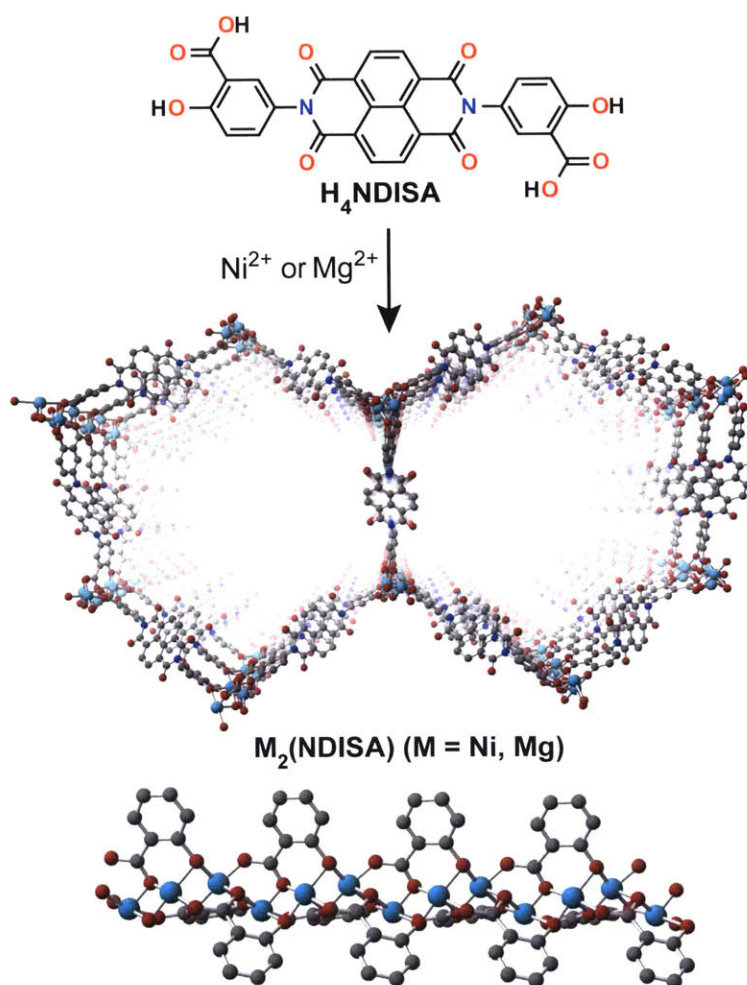


**Figure 2.1.** Synthesis and simulated structure of **M-NDISA** viewed along the *c* axis. A representation of the secondary building unit is shown. Teal, blue, red, and grey spheres represent metal (Mg or Ni), N, O, and C atoms, respectively. H atoms are omitted for clarity.

### c. Thin film deposition

**Mg-NDISA** and **Ni-NDISA** exhibit different morphologies when deposited as thin films. When **Mg-NDISA** is grown on fluorine-doped tin oxide (FTO) glass under conditions mimicking its bulk synthesis, only thick, non-uniform powders are deposited. However, uniform films of **Mg-NDISA** can be deposited on FTO using an anhydrous mixture of DMF and methanol at 120 °C, as confirmed by PXRD analysis (Figures 2.2 and S2). Scanning electron



microscopy (SEM) revealed a fiber-like morphology for these films, with features as thin as approximately 25 nm. This morphology contrasts with that observed for **Ni-NDISA** films, which are much denser and uniform, despite being deposited under identical conditions to the **Mg-NDISA** films.

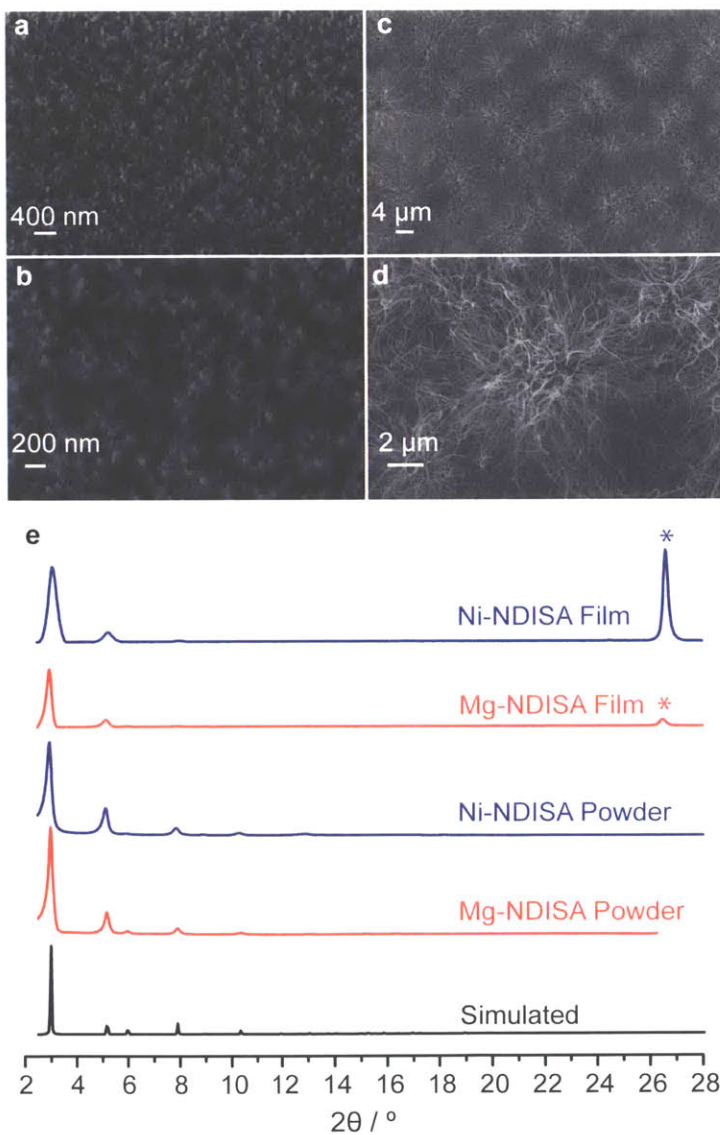


**Figure 2.2.** Scanning electron micrographs of (a,b) **Ni-NDISA** (at 400 nm and 200 nm magnifications, respectively) and (c,d) **Mg-NDISA** (at 4 μm and 2 μm magnifications, respectively) thin films. (e) Simulated and experimental PXRD patterns of **Mg-NDISA** and **Ni-NDISA** powders and thin-films (peaks labeled with \* correspond to FTO).



Clearly, the difference in morphology stems from the different rates of nucleation and growth for the two materials: the Ni material likely nucleates much faster and thus produces denser films than its Mg analog, whose growth appears to dominate overall film deposition. Faster nucleation may also be responsible for rapid precipitation of **Ni-NDISA**, which can be isolated within approximately 15 minutes, whereas **Mg-NDISA** requires an induction period of at least 40 minutes. The different relative rates of nucleation and growth for the two materials, which affect the morphology of their thin films, have a profound effect on the optical properties of the films, as discussed below.

#### d. Electrochemical and spectroelectrochemical studies

**Table 2.1.** Redox potentials for **Mg-NDISA**, **Ni-NDISA**, and **H<sub>4</sub>NDISA**<sup>a</sup>

	$[\text{NDI}]/[\text{NDI}]^{\cdot-}$	$[\text{NDI}]^{\cdot-}/[\text{NDI}]^{2-}$
	$E_{1/2}$ [V]	$E_{1/2}$ [V]
<b>Mg-NDISA</b>	-1.1	-1.7
<b>Ni-NDISA</b>	-1.2	-1.9
<b>H<sub>4</sub>NDISA</b>	-1.0	-1.4

<sup>a</sup>All potentials are reported vs. Fc/Fc<sup>+</sup>. See Figures S3 and S4 for CV curves.

Both **Mg-NDISA** and **Ni-NDISA** films exhibit two quasi-reversible one-electron redox couples (Table 1, Figure S3). The first and second reduction peaks are consistent with the formation of the radical anion  $[\text{NDI}]^{\cdot-}$  and dianion  $[\text{NDI}]^{2-}$ , respectively. The cathodic shift in the reduction potentials observed for the thin films relative to the free ligand (Table 1, Figure S4) could be due to the immobilization of the ligand inside the MOF and/or differences between solution and solid-state kinetics, as brought by either electrolyte diffusion limitations, or by electron hopping within the MOF skeleton. Nevertheless, attesting to the stability of the new MOFs to redox reactivity, both films showed excellent stability to CV cycling with no observable decrease in crystallinity up to 10 cycles (See Figures S5, and S6).

We sought to investigate the utility of **Mg-NDISA** and **Ni-NDISA** as electrochromic materials by measuring their absorption spectra during electrochemical cycling. Notably, because both materials can be deposited as thin films, both films are transparent when the NDI ligands are in their neutral state, and both turn dark upon reduction. However, because of their mesh/fiber-like morphology, **Mg-NDISA** films exhibit significant scattering, which reduces their optical quality and therefore limits their practical applications (Figure S7). As such, spectroelectrochemical investigations were performed only on **Ni-NDISA** films, which exhibit no observable scattering. As shown in Figure S8, a UV-Vis spectrum of the free ligand, H<sub>4</sub>NDISA, in DMF closely matches that of **Ni-NDISA** films in their neutral state. Both are dominated by the strong  $\pi \rightarrow \pi^*$  transitions of the NDI core, with  $\lambda_{\text{max}}$  at 362 nm and 383 nm. The **Ni-NDISA** film exhibited fast color changes at a constant potential of  $-2.0$  V (versus Fc/Fc<sup>+</sup>) (Figure 2.3). The absorption spectrum, collected at 1 s intervals, revealed the complete formation of [NDI]<sup>-</sup> species after 7 s, followed by formation of doubly reduced [NDI]<sup>2-</sup> cores after an additional 23 s. The dark states of the reduced films are due to the intense absorptions across the visible spectrum centered at  $\lambda_{\text{max}} = 475$  nm, 700 nm, and 772 nm for [NDI]<sup>-</sup>, and 397 nm, 423 nm, and 560 nm for [NDI]<sup>2-</sup>. We note that the width of the  $\lambda_{\text{max}}$  peak for NDI in its singly reduced state extends wider than for the doubly reduced state.

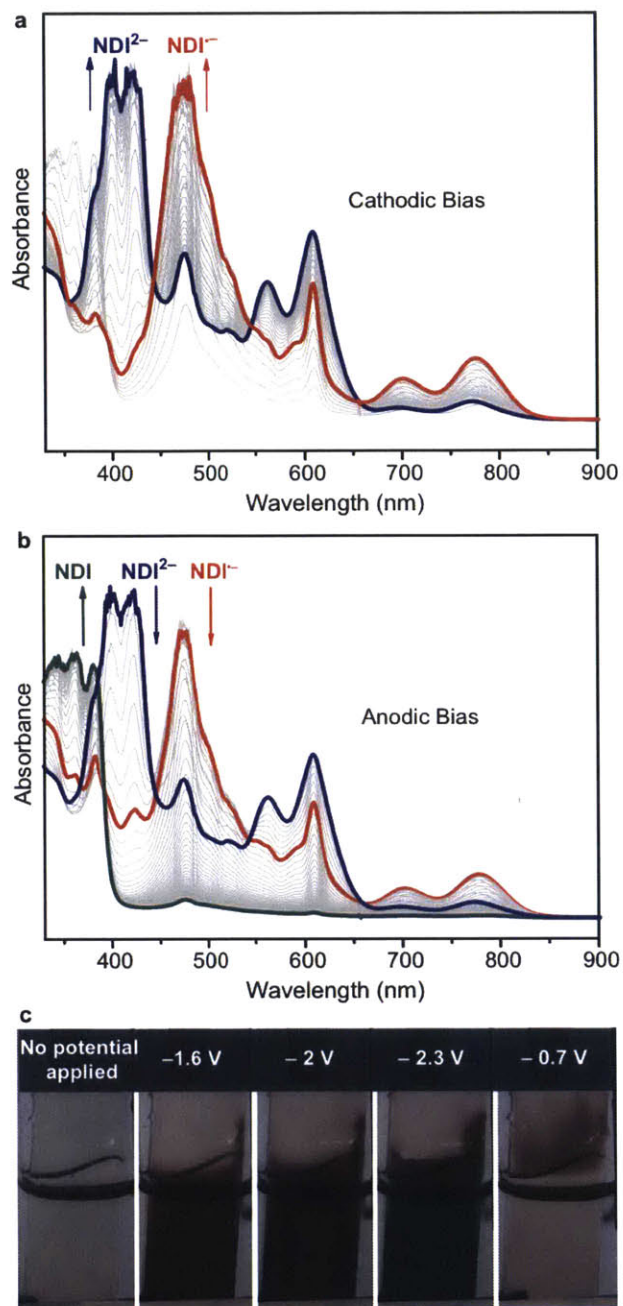


**Figure 2.3.** Spectroelectrochemical data of Ni-NDISA collected by transmission UV/Vis spectroscopy showing the reversible formation of [NDI]<sup>-</sup> and [NDI]<sup>2-</sup> when (a)  $-0.5\text{ V} \rightarrow -2\text{ V}$  reducing and (b)  $-2\text{ V} \rightarrow -0.5\text{ V}$  oxidizing step-potentials are applied (vs. Fc/Fc<sup>+</sup>). (c) Images of reversible color switching of Ni-NDISA films at several reducing potentials ( $-1.6\text{ V}$ ,  $-2\text{ V}$ , and  $-2.3\text{ V}$  vs. Fc/Fc<sup>+</sup>). Complete reversibility to the neutral transparent state is achieved by applying a reverse anodic bias ( $-0.7\text{ V}$  vs. Fc/Fc<sup>+</sup>). All measurements were performed in  $0.1\text{ M}$  [(<sup>t</sup>Bu)<sub>4</sub>N]PF<sub>6</sub>/DMF solution using a three-electrode setup, and the UV/Vis spectra were collected at 1 second intervals (see Experimental Procedures for details).

Because the singly reduced state can be reached with an applied potential of only  $\sim 1$  V in a two-electrode device, as expected based on the CV in Figure S3, a low power consumption should be expected for devices made from **Ni-NDISA**. Furthermore, because  $[\text{NDI}]^-$  and  $[\text{NDI}]^{2-}$  have almost complementary absorption profiles across the visible spectrum, **Ni-NDISA** films become nearly black at potentials where the ratio of  $[\text{NDI}]^-$  to  $[\text{NDI}]^{2-}$  is approximately 1:1 (See Figure 2.3 and supplemental movies). Complete recovery of the transparent, neutral material upon applying an anodic potential confirms that the **Ni-NDISA** films exhibit fully reversible electrochromic behavior. Finally, the mesoporosity of **Ni-NDISA**, which is necessary for fast electrolyte transport within the material, was confirmed by measuring  $\text{N}_2$  uptake isotherms on the activated bulk powder. As shown in Figure S9, **Ni-NDISA** displays a type IV isotherm with high  $\text{N}_2$  uptake at 77 K, consistent with the presence of mesoporous channels. Fitting the  $\text{N}_2$  adsorption isotherm to the BET equation gave an apparent surface area of  $1722 \pm 9 \text{ m}^2/\text{g}$ , in line with previous MOF-74 analogs with similar pore sizes.<sup>7a</sup>

#### **e. Discussion and summary**

Switching between the neutral and singly reduced state of **Ni-NDISA**, 7 s under our conditions, is faster than that of transition metal oxides (e.g.  $\text{WO}_3$ ), which typically exhibit switching times of multiple seconds to minutes,<sup>11,12</sup> and is comparable to some of the reported polymeric electrochromic materials.<sup>12</sup> However, a reasonable comparison with other electrochromic materials can only be attained in cases where experimental setup and thin film growth conditions are identical. We thus expect that it is possible to improve the switching times for **Ni-NDISA** by optimizing the device construction, the electrolyte, and the quality of films. Although the intense absorption of the **Ni-NDISA** films caused deviations from a linear absorption response, thereby preventing the determination of a reliable coloration efficiency (CE), it is reasonable to

assume that these films exhibit CE values similar to those reported for previous NDI-based electrochromic MOFs,<sup>2a</sup> which exceeded  $100 \text{ cm}^2\text{C}^{-1}$  in the blue region of the spectrum.

In conclusion, synthesis of a new salicylate-functionalized naphthalene-diimide ligand led to the isolation of two new mesoporous MOFs with the MOF-74 topology that display ligand-based redox activity. We developed strategies for the deposition of thin films of  $\text{Ni}_2(\text{NDISA})$  and  $\text{Mg}_2(\text{NDISA})$ , which exhibit morphologies that are highly dependent on their relative rates of nucleation and growth. **Ni-NDISA** films exhibit fast electrochromic switching from transparent to dark, a desirable feature for electrochromic materials, with potential applications in optoelectronic devices. Beyond electrochromism, our strategy for the formation of mesoporous MOFs bearing ligands with reversible multi-electron redox couples may find applications in energy storage devices, especially when combined with redox-active metals.

#### **f. Experimental procedures and supplementary information.**

**General Considerations.** 1,4,5,8-Naphthalenetetracarboxylic dianhydride (Alfa Aesar, 97%), 5-amino-2-hydroxybenzoic acid (Matrix Scientific, 97%)  $\text{Mg}(\text{NO}_3)_2 \cdot 6\text{H}_2\text{O}$  (Alfa Aesar),  $\text{Ni}(\text{NO}_3)_2 \cdot 6\text{H}_2\text{O}$  (Strem Chemicals, 99.9985%), methanol (Sigma Aldrich), ethanol (Koptec, 100%), and *N,N*-dimethylformamide (DMF, 99.9%, EMD Millipore) were used as received unless otherwise noted. DMF was additionally dried and deoxygenated using a Glass Contour solvent purification system fitted with  $\text{Al}_2\text{O}_3$  drying columns. Tetra-*n*-butylammonium hexafluorophosphate (99 %, Fluka) was dried in vacuo at 85 °C before use. Fluorine-doped tin oxide (FTO)-coated glass slides were purchased from Hartford Glass and cleaned by washing sequentially with distilled water, acetone (sonication for 1 min), and ethanol (sonication for 15 min). Bis(cyclopentadienyl)iron (Ferrocene, Fc, Strem Chemicals, 99%) was used for the

determination of the redox potential of Fc/Fc<sup>+</sup> couple in electrochemical measurements.

A CHI 600D potentiostat/galvanostat (CH instruments, Inc.) was used for cyclic voltammetry and spectroelectrochemical measurements. All electrochemical measurements were carried out in a nitrogen glovebox or in sealed cells under a flow of nitrogen gas. Powder X-ray diffraction (PXRD) patterns were collected on a Bruker Advance D8 diffractometer using Nickel-filtered Cu-K<sub>α</sub> radiation ( $\lambda = 1.5418 \text{ \AA}$ ). SEM images were obtained with a FESEM Ultra55 microscope at acceleration voltage of 5 kV. UV-Vis absorption spectra were measured using an Agilent 8453 UV-visible transmission spectrometer (Agilent Technologies) equipped with a halogen and deuterium light sources. A Micromeritics ASAP 2020 Surface Area and Porosity Analyzer was used to measure N<sub>2</sub> adsorption isotherms.

**Cyclic voltammetry (CV).** Measurements were carried out in a degassed DMF solution containing 0.1 M [(nBu)<sub>4</sub>N]PF<sub>6</sub> using three-electrode electrochemical cells with the FTO substrate as the working electrode, platinum mesh as counter electrode, and a platinum electrode (Pt disc) as pseudo-reference electrode (calibrated against the Fc/Fc<sup>+</sup> couple). In order to ensure a stable potential from the pseudo-reference electrode, the films were cycled several times before the final CV was obtained and calibrated against Fc/Fc<sup>+</sup> couple.

**Spectroelectrochemistry.** Measurements were conducted in a sealed transparent glass cell under nitrogen flow in a degassed DMF solution containing 0.1 M [(nBu)<sub>4</sub>N]PF<sub>6</sub> using three-electrode setup with the FTO substrate as the working electrode, platinum mesh as counter electrode, and a platinum electrode (Pt disc) as pseudo-reference electrode (calibrated against Fc/Fc<sup>+</sup> couple). The UV/Vis spectra of **Ni-NDISA** films were obtained by applying constant step-potential from  $-0.5 \text{ V} \rightarrow -2 \text{ V}$  (vs. Fc/Fc<sup>+</sup>) and measuring the spectra at constant time intervals (1 second).

**M-NDISA Structure Simulation.** M-NDISA structures were simulated starting from the reported structure of IRMOF-74-IV.<sup>7a</sup> NDISA was introduced in place of the original linker in the reported MOF and the SBU was modified to take into account the difference in connectives between NDISA and the original linker. No solvent molecules were included in the model. The unit cell parameters were then refined against the experimental pattern by performing Pawley refinement in Materials Studio (Materials Studio v. 5.0.0.0, 2009, Accelrys Software Inc.). The simulated PXRD and structure are in the trigonal  $R\bar{3}$  space group; however, both  $R3$  and  $R\bar{3}$  space groups fit equally well. The pore diameter was then determined by measuring the van der Waals distance between two open-metal sites. Both Mg-NDISA and Ni-NDISA gave similar lattice parameters.

**Gas sorption measurements.** Oven-dried sample tubes equipped with TranSeals™ (Micromeritics) were evacuated and tared. Samples were transferred to the sample tube, which was then capped by a TranSeal™. The evacuated sample tubes were weighed again, and the sample mass was determined by subtracting the mass of the previously tared tubes. N<sub>2</sub> isotherms were measured with grade 5.0 N<sub>2</sub> gas using a liquid nitrogen bath (77 K).

**Synthesis of *N,N'*-bis(3-carboxy-4-hydroxyphenyl)-1,4,5,8 naphthalenetetracarboximide (H<sub>4</sub>NDISA).**

A dry 100 mL Schlenk flask was charged with 1,4,5,8-naphthalenetetracarboxylic dianhydride (1.0 g, 3.7 mmol), 5-amino-2-hydroxybenzoic acid (1.2 g, 7.8 mmol), and anhydrous DMF (35 mL) under a nitrogen atmosphere. The reaction mixture was heated at 130 °C with rapid stirring for 1 day. The flask was cooled to room temperature and the orange suspension was filtered off and washed with DMF, diethyl ether, and methanol, then dried *in vacuo* to afford 1.5 g (70 %) of orange powder. We note that at this stage, the solid is isolated with one molecule of dimethyl

amine ( $\text{HN}(\text{CH}_3)_2$ ) per molecule of NDISA, and was used in this form for further synthesis (the reported yield takes the presence of  $\text{HN}(\text{CH}_3)_2$  into account). In order to obtain the pure form of the solid, an additional wash with  $\sim 30$  mL 2 M HCl for 1 day is necessary.  $^1\text{H}$  NMR (400 MHz;  $\text{dms}\text{-}d_6$ ):  $\delta$  8.71 (4H, s), 8.35 (2H, s), 7.805 (2H, d,  $J = 2.8$  Hz), 7.40 (2H, dd,  $J_1 = 8.6$  Hz,  $J_2 = 2.4$ ), 6.96 (2H, d,  $J = 8.4$  Hz), 2.55 (6H, ( $\text{HN}(\text{CH}_3)_2$ ), s).  $^{13}\text{C}$  NMR (600 MHz;  $\text{dms}\text{-}d_6$ ):  $\delta$  171.16, 163.05, 161.68, 134.07, 130.49, 130.25, 126.96, 126.58, 125.11, 116.79, 116.49, 34.21 ( $\text{HN}(\text{CH}_3)_2$ ). Elemental analysis calcd. for  $\text{C}_{30}\text{H}_{21}\text{N}_3\text{O}_{10}$ : C, 61.71; H, 3.68; N, 7.30. Found: C, 61.39; H, 3.76; N, 7.15. This corresponds to a formula of  $\text{H}_4\text{NDISA}\cdot\text{HN}(\text{CH}_3)_2$

**Synthesis of  $[\text{Mg}_2(\text{C}_{28}\text{H}_{10}\text{N}_2\text{O}_{10})(\text{H}_2\text{O})_2]\cdot 2.4(\text{H}_2\text{O})$  (Mg-NDISA) powder.** A 20 mL vial was charged with NDISA (55 mg, 0.094 mmol),  $\text{Mg}(\text{NO}_3)_2\cdot 6\text{H}_2\text{O}$  (80 mg, 0.31 mmol), and DMF:ethanol:water (7.5 mL:0.5 mL:0.5 mL). The reaction mixture was heated at 120 °C for 1 day. After allowing the reaction to cool to room temperature, the precipitated solids were separated by filtration and washed with DMF. The solids were then placed in 20 mL methanol for three days where the solvent was decanted and refilled at least 3 times. The solids were then evacuated in a Tousimis Samdri PVT-3D critical point dryer; the methanol containing samples were completely exchanged with liquid  $\text{CO}_2$ . Then, the chamber containing the solids and liquid  $\text{CO}_2$  was heated to 40 °C to achieve supercritical conditions and held under those conditions for approximately 20 min. Finally, the chamber was slowly vented (20 min) to obtain crystalline solids. The samples were always kept solvated before the  $\text{CO}_2$  drying step. Samples for combustion elemental analysis (C, H, N) were heated to 40 °C under vacuum for 24 h. Elemental analysis calcd. for  $\text{Mg}_2(\text{C}_{28}\text{H}_{18.8}\text{N}_2\text{O}_{14.4})$ : C, 50.8; H, 2.86; N, 4.23. Found: C, 50.8; H, 2.79; N 4.13.



**Synthesis of  $[\text{Ni}_2(\text{C}_{28}\text{H}_{10}\text{N}_2\text{O}_{10})(\text{H}_2\text{O})_2]\cdot 4(\text{H}_2\text{O})$  (Ni-NDISA) powder.** A 20 mL vial was charged with NDISA (55 mg, 0.094 mmol),  $\text{Ni}(\text{NO}_3)_2\cdot 6\text{H}_2\text{O}$  (104 mg, 0.36 mmol), and DMF:ethanol:water (7.5 mL:0.5 mL:0.5 mL). The reaction mixture was heated at 120 °C for 1 day. After allowing the reaction to cool to room temperature, the precipitated solids were separated by filtration and washed with DMF. The solids were then placed in 20 mL methanol for three days where the solvent was decanted and refilled at least 3 times. The solids were then evacuated in a Tousimis Samdri PVT-3D critical point dryer; the methanol containing samples were completely exchanged with liquid  $\text{CO}_2$ . Then, the chamber containing the solids and liquid  $\text{CO}_2$  was heated to 40 °C to achieve supercritical conditions and held under those conditions for approximately 20 min. Finally, the chamber was slowly vented (20 min) to obtain crystalline solids. The samples were always kept solvated before the  $\text{CO}_2$  drying step. Samples for combustion elemental analysis (C, H, N) were placed under high vacuum ( $10^{-6}$  torr) for 6 h. Elemental analysis calcd. for  $\text{Ni}_2(\text{C}_{28}\text{H}_{22}\text{N}_2\text{O}_{16})$  C, 44.26; H, 2.92; N, 3.69. Found: C, 43.87; H, 2.27; N 3.46. Before the gas adsorption measurement of **Ni-NDISA**, the sample was placed under high vacuum ( $10^{-6}$  torr) at 100 °C for 1 day.

**Synthesis of M-NDISA (M =  $\text{Mg}^{2+}$ ,  $\text{Ni}^{2+}$ ) films on FTO.**  $\text{H}_4\text{NDISA}$  (55 mg, 0.094 mmol) and  $\text{Mg}(\text{NO}_3)_2\cdot 6\text{H}_2\text{O}$  (80 mg, 0.31 mmol) or  $\text{Ni}(\text{NO}_3)_2\cdot 6\text{H}_2\text{O}$  (90 mg, 0.31 mmol) were dissolved in anhydrous DMF (10 mL) and anhydrous methanol (1 mL) in a 20 mL vial. Precleaned FTO substrate (see general considerations in the SI for details) was submerged in the solution with the conductive side facing downwards. The solution was then heated to 120 °C in a convection oven for 40 min in the case of **Mg-NDISA** and for 30 min in the case of **Ni-NDISA**. All manipulations were done under ambient conditions. After allowing the reaction to cool to room temperature, the substrates were removed, soaked and washed with fresh DMF, and any solids attached to the

non-conductive side were removed with a DMF-wet q-tip. The substrates were then submerged in a vial containing methanol (20 mL) for at least 3 hours and up to 1 day before evacuation. The films were then evacuated in Tousimis Samdri PVT-3D critical point dryer (see the section above for CO<sub>2</sub> drying details). The samples were always kept solvated before the CO<sub>2</sub> drying step.

**Scheme S1.** Synthesis of *N,N'*-bis(3-carboxy-4-hydroxyphenyl)-1,4,5,8-naphthalenetetracarboximide ( $H_4$ NDISA). Scheme S1 is related to the synthetic procedure of  $H_4$ NDISA in the Experimental Procedures.

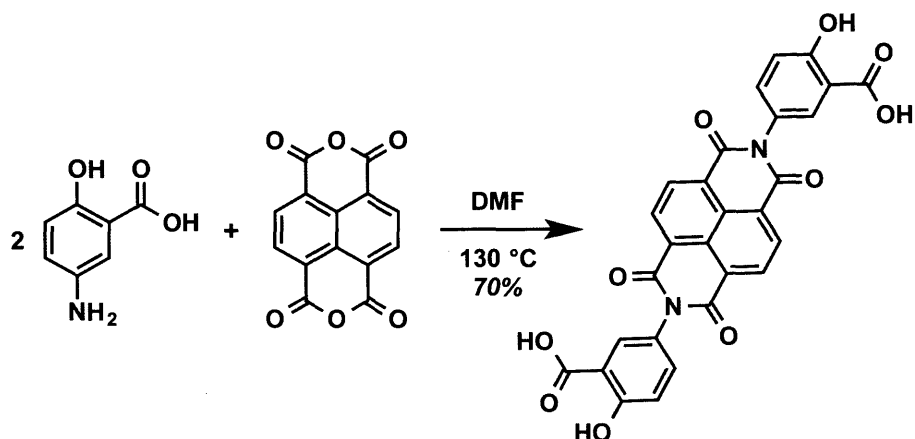


**Table S1.** Summary of cell parameters and Pawley refinement details for **M-NDISA**. Table S1 is related to Figures 2.1 and 2.2.

	Mg-NDISA	Ni-NDISA
<b>Empirical Formula</b>	$Mg_2(C_{28}H_{18.8}N_2O_{14.4})$	$Ni_2(C_{28}H_{22}N_2O_{16})$
<b>Space Group</b>	$R3$ or $R\bar{3}$	$R3$ or $R\bar{3}$
<b><i>a</i> (Å)</b>	$59.356 \pm 0.004$	$59.798 \pm 0.007$
<b><math>R_{wp}</math></b>	5.9%	7.98%

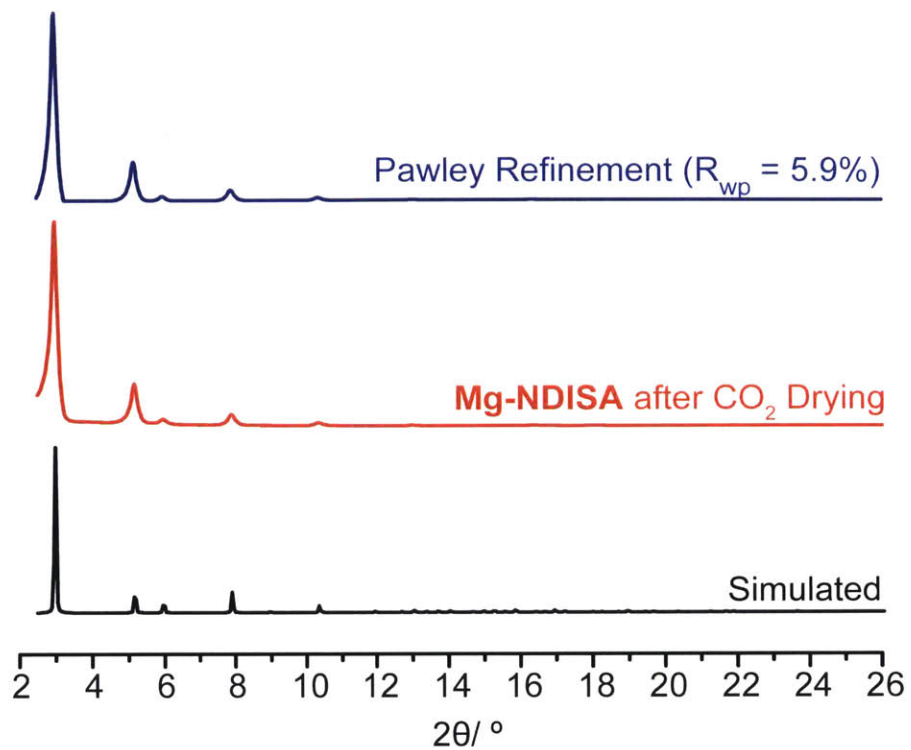


**Figure S1.** Simulated, experimental, and Pawley refined PXR D patterns of **Mg-NDISA**. Figure S1 is related to Figures 2.1 and 2.2 and structure simulation in the Experimental Procedures.

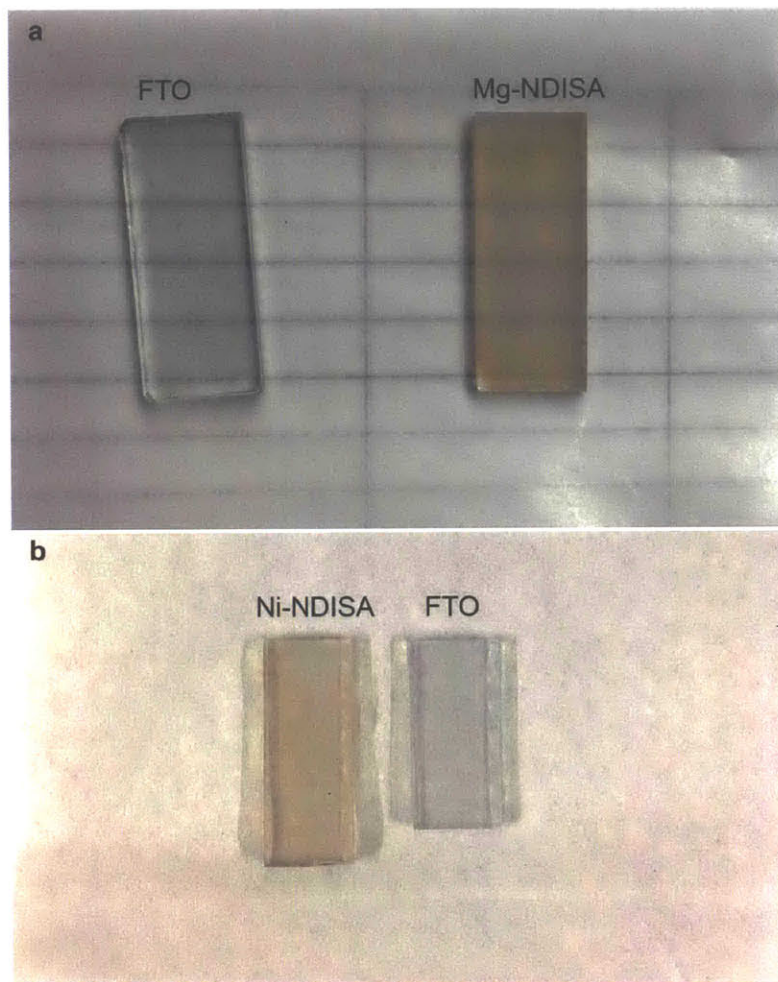


**Figure S2.** Dry thin films of **Mg-NDISA** (a) and **Ni-NDISA** (b) deposited on 1 cm-wide FTO slides from anhydrous mixtures of DMF: methanol (10:1). Blank FTO slides are shown for comparison. Figure S2 is related to Figure 2.2.

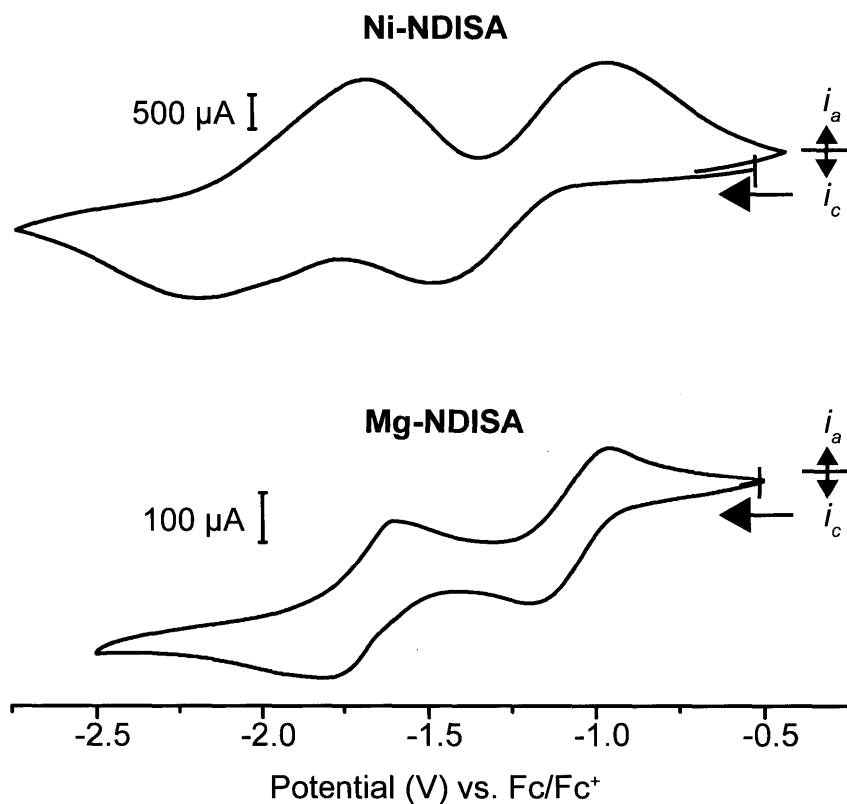


**Figure S3.** Cyclic voltammogram of **Ni-NDISA** and **Mg-NDISA** films in 0.1 M [(<sup>n</sup>Bu)<sub>4</sub>N]PF<sub>6</sub> at a scan rate of 0.1 V/s with FTO as working electrode, platinum electrode as pseudo-reference electrode, and platinum mesh as counter electrode. Potentials are reported against (Fc/Fc<sup>+</sup>). The open-circuit potential is noted with a vertical line in each voltammogram. Figure S3 is related to Table 2.1.

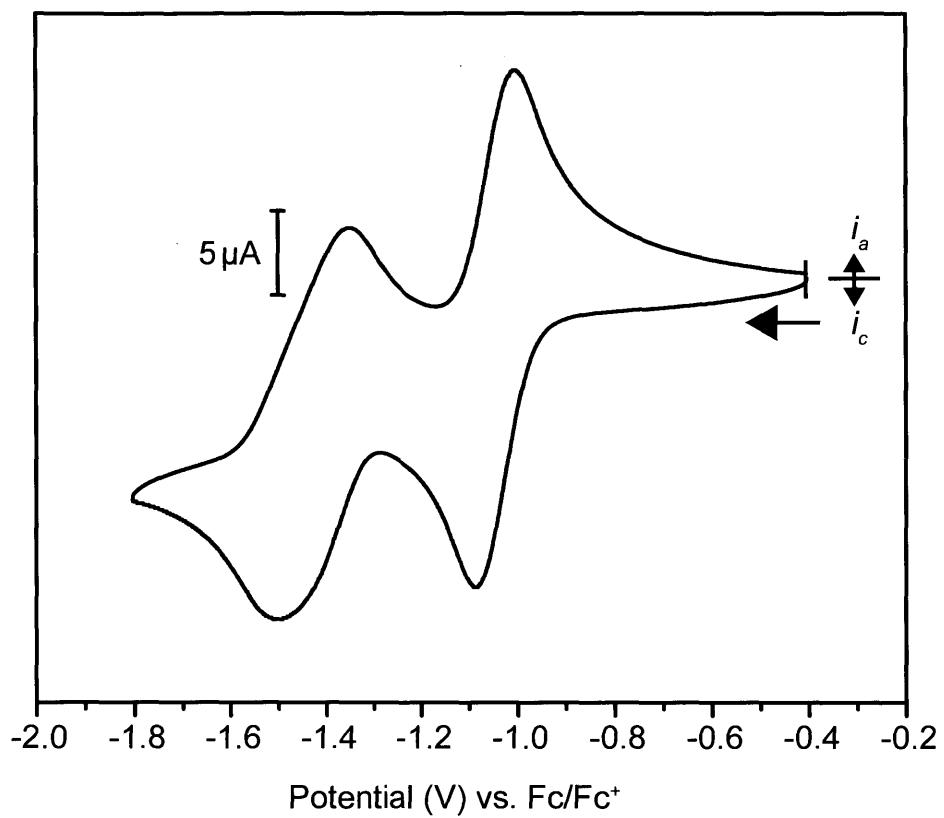


**Figure S4.** Cyclic voltammogram of H<sub>4</sub>NDISA. Figure S4 is related to Table 2.1.

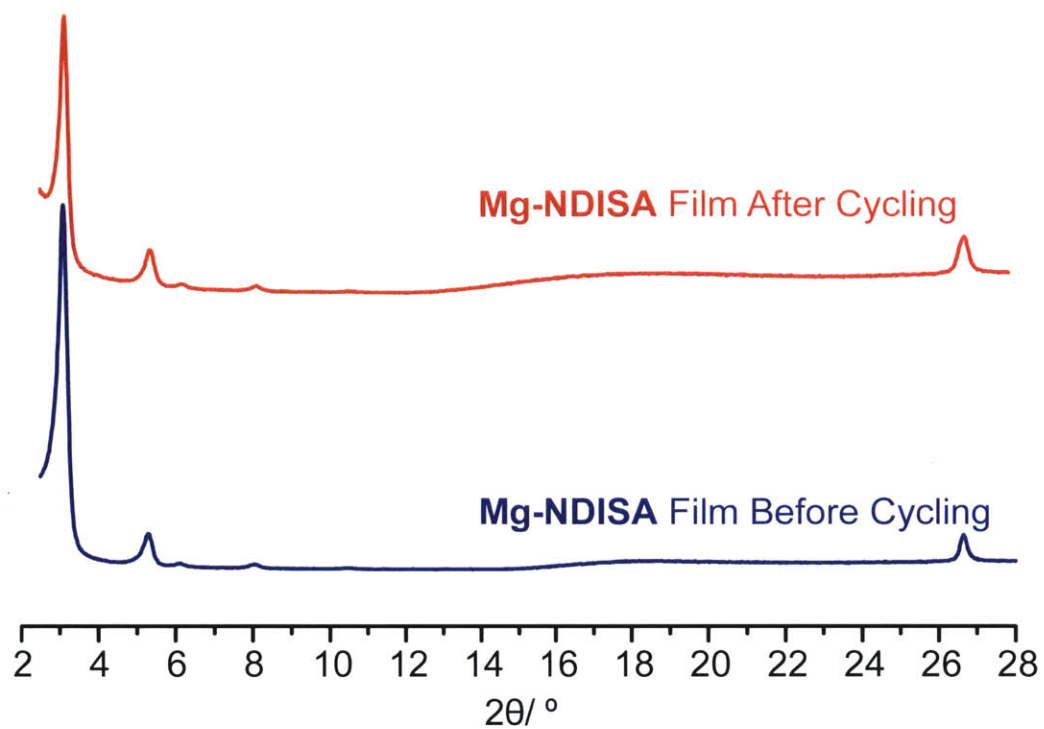


**Figure S5.** PXRD pattern of **Mg-NDISA** before and after electrochemical cycling (10 CV cycles at 0.1 V/s). Figure S5 is related to Figure 2.2 and Table 2.1.



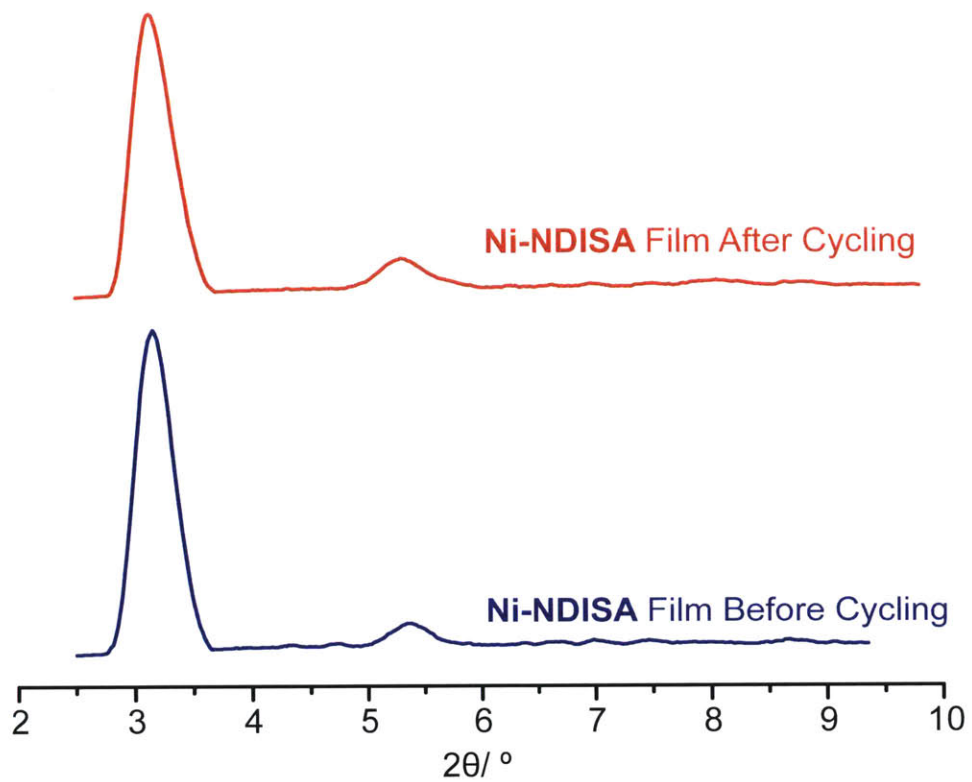


**Figure S6.** PXRD pattern of **Ni-NDISA** before and after 6 CV cycles at 0.1 V/s. Figure S6 is related to Figure 2.2 and Table 2.1.

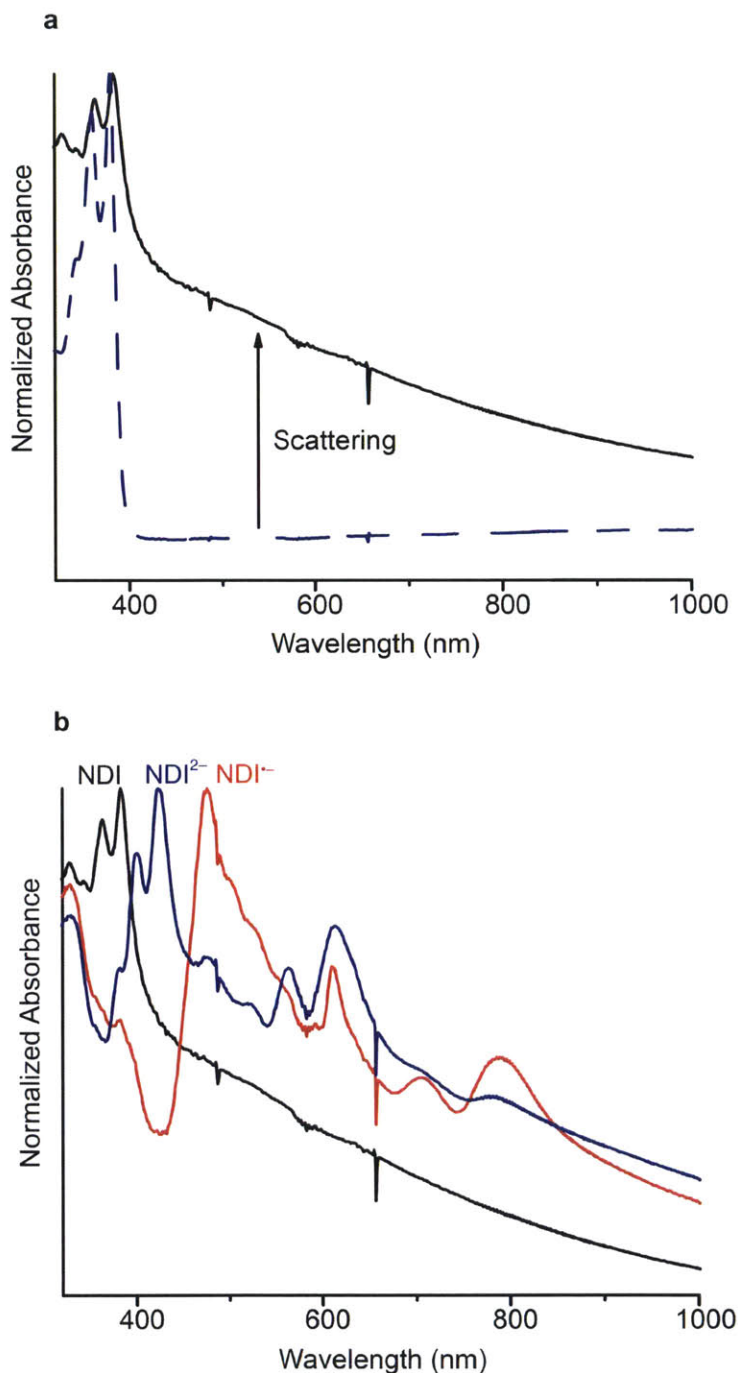


**Figure S7.** (a) Normalized UV/Vis absorbance spectra of **Mg-NDISA** film (black) and H<sub>4</sub>NDISA in DMF (dashed blue). (b) Spectroelectrochemistry of **Mg-NDISA** showing the generation of [NDI]<sup>•-</sup> and [NDI]<sup>2-</sup> upon applying a reducing potential. Significant scattering is observed from the **Mg-NDISA** film in both the neutral and reduced forms. Figure S7 is related to spectroelectrochemical measurements in the Experimental Procedures.

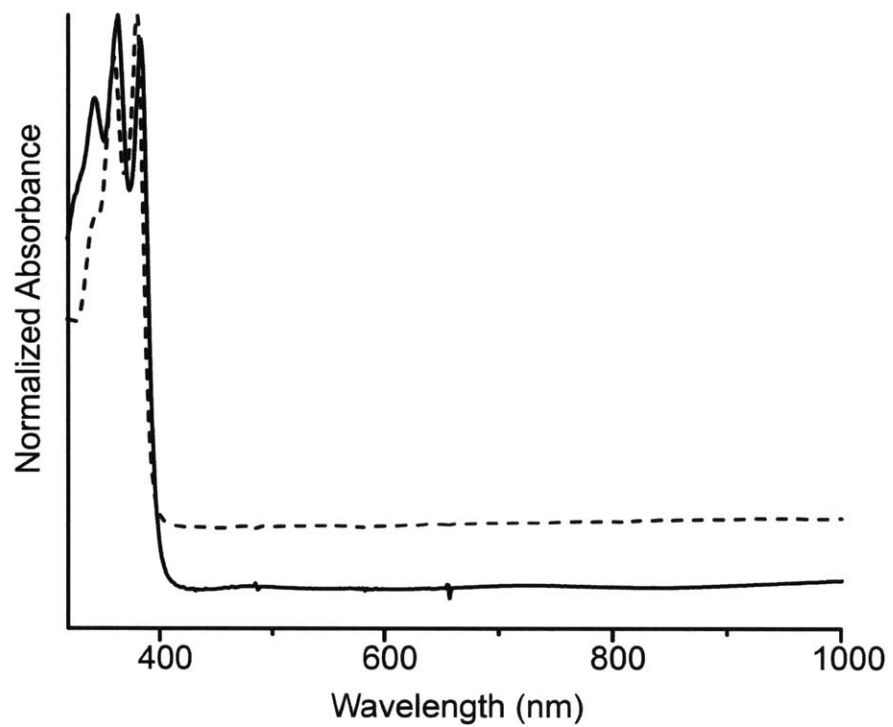


**Figure S8.** Normalized UV/Vis absorbance spectra of Ni-NDISA film (solid line) and H<sub>4</sub>NDISA in DMF (dashed line). Figure S8 is related to Figure 2.3.

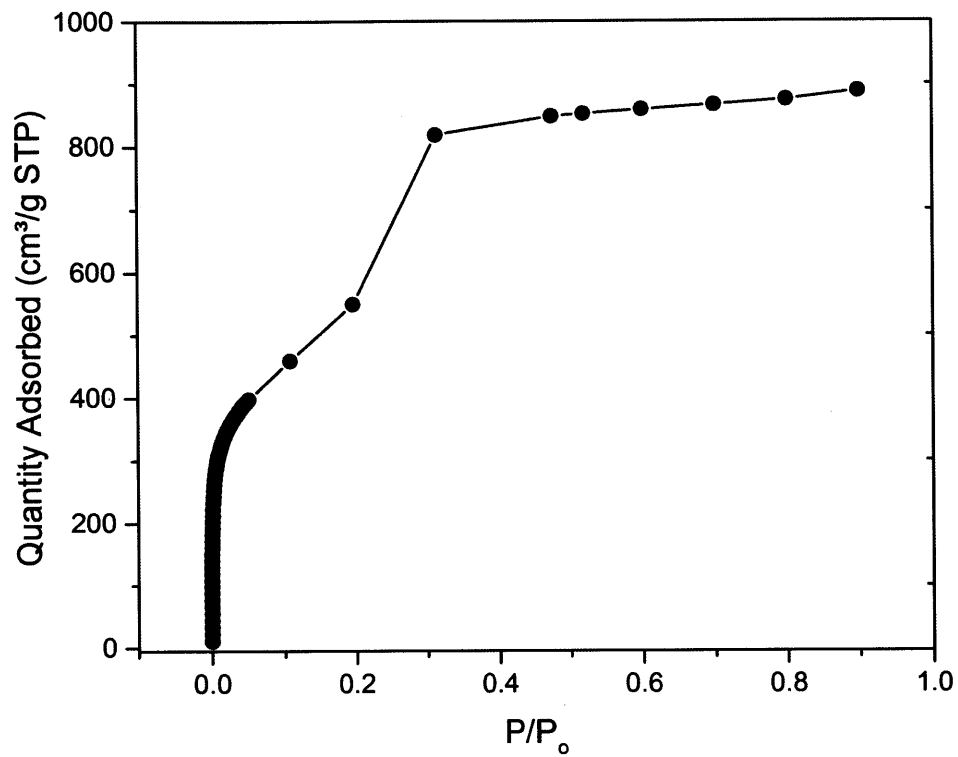


**Figure S9.** N<sub>2</sub> adsorption isotherm for Ni-NDISA powder measured at 77 K. Figure S9 is related to the gas sorption measurements in the Experimental Procedures.

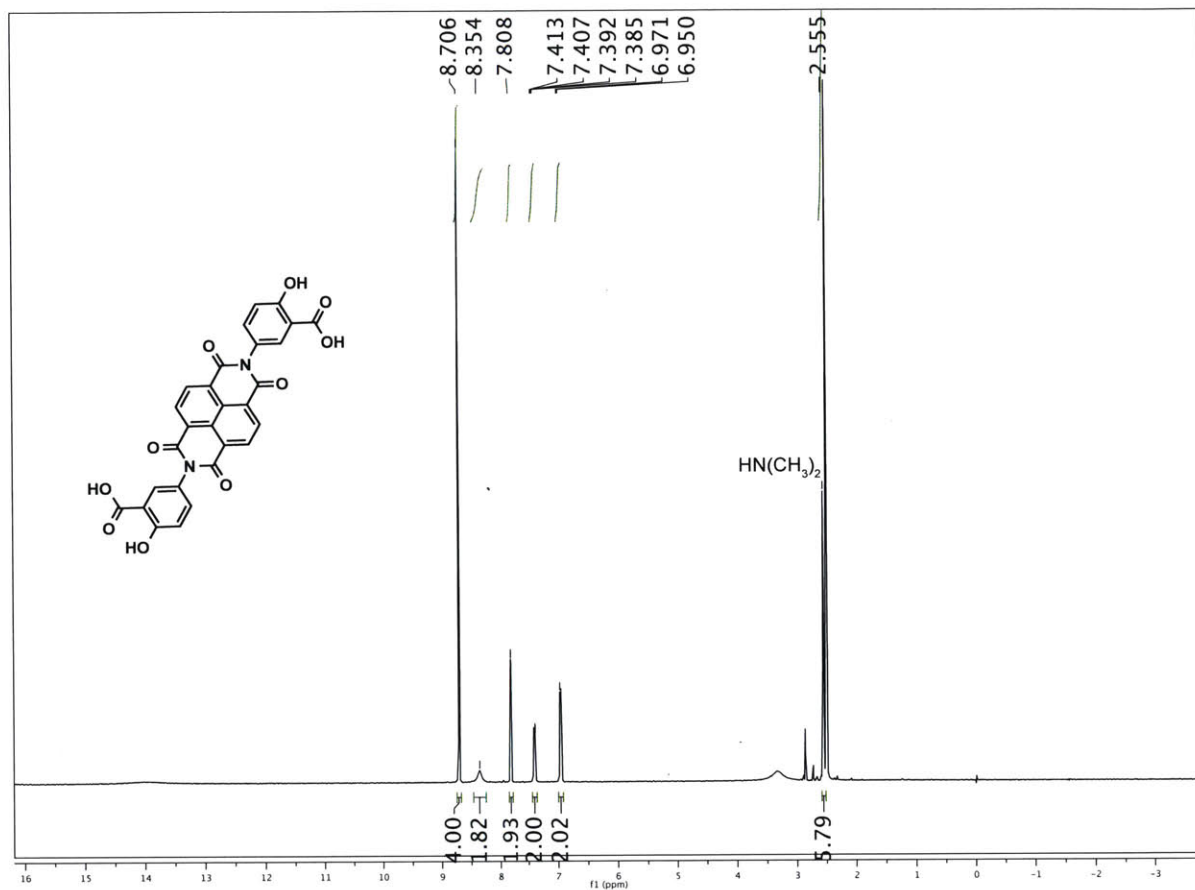


**Figure S10.** <sup>1</sup>H NMR of H<sub>4</sub>NDISA. Figure S10 is related to the synthetic procedure of H<sub>4</sub>NDISA in the Experimental Procedures.

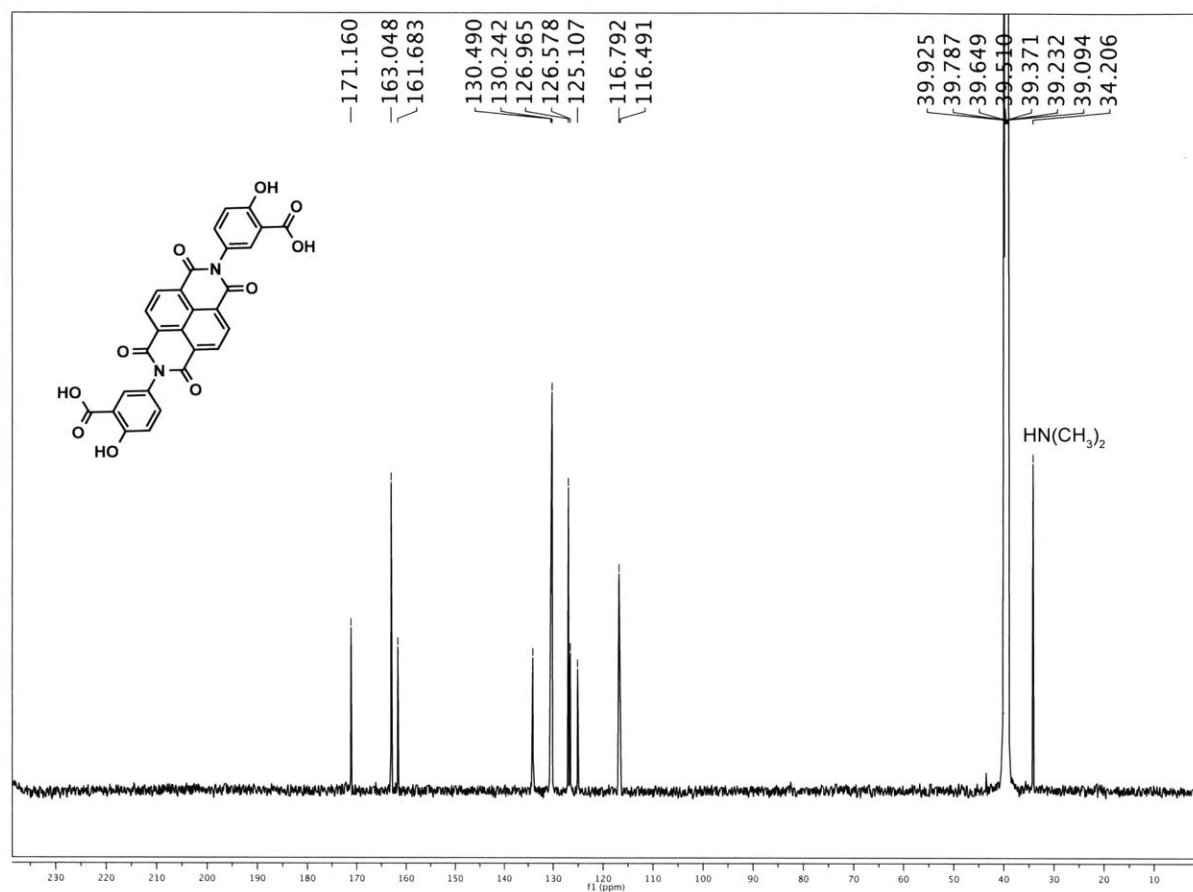


**Figure S11.** <sup>13</sup>C NMR of H<sub>4</sub>NDISA. Figure S11 is related to the synthetic procedure of H<sub>4</sub>NDISA in the Experimental Procedures.

### **g. Author contributions and acknowledgments**

K.A. performed experiments. C.R.W. performed preliminary experiments with H<sub>4</sub>NDISA. K.A. and M.D. devised experiments, interpreted data, and wrote the paper.

This work was supported by the Cooperative Agreement between the Masdar Institute of Science and Technology (Masdar Institute), Abu Dhabi, UAE and the Massachusetts Institute of Technology (MIT), Cambridge, MA, USA - Reference 02/MI/MIT/CP/11/07633/GEN/G/00 and as part of the Center for Excitonics, an Energy Frontier Research Center funded by the U.S. Department of Energy, Office of Science, Office of Basic Energy Sciences, under award no. DE-SC0001088 (MIT). K.A. acknowledges Saudi Aramco for financial support during graduate studies. We thank Dr. M. G. Campbell and Dr. D. Sheberla for insightful discussions. We thank Dr. D. Sheberla for assistance with image processing and Dr. Y. Tulchinsky for assistance with <sup>13</sup>C NMR.

## h. References and notes

<sup>1</sup> a) Kornienko, N.; Zhao, Y.; Kley, C. S.; Zhu, C.; Kim, D.; Lin, S.; Chang, C. J.; Yaghi, O. M.; Yang, P. (2015) Metal–Organic Frameworks for Electrocatalytic Reduction of Carbon Dioxide *J. Am. Chem. Soc.* 137, 14129–14135. b) Ahrenholtz, S. R.; Epley, C. C.; Morris, A. J. (2014) Solvothermal Preparation of an Electrocatalytic Metalloporphyrin MOF Thin Film and its Redox Hopping Charge-Transfer Mechanism. *J. Am. Chem. Soc.* 136 (6), pp 2464–2472

<sup>2</sup> a) Wade, C. R.; Li, M.; Dincă, M. (2013) Facile Deposition of Multicolored Electrochromic Metal–Organic Framework Thin Films. *Angew. Chem., Int. Ed.* 52 (50), 13377–13381. b) Garai, B.; Mallick, A.; Banerjee, R. (2016) Photochromic Metal–Organic Frameworks for Inkless and Erasable Printing. *Chem. Sci.* 7, 2195–2200. c) Usov, P. M.; Fabian, C.; D'Alessandro, D. M. (2012) Rapid Determination of the Optical and Redox Properties of a Metal–Organic Framework *via in situ* Solid State Spectroelectrochemistry. *Chem. Comm.* 48(33), 3945–3. d) Kung, C. W.; Wang, T. C.; Mondloch, J. E.; Fairen-Jimenez, D.; Gardner, D. M.; Bury, W.; Klingsporn, J. M.; Barnes, J. C.; Van Duyne, R.; Stoddart, J. F.; Wasielewski, M. R.; Farha, O. K.; Hupp, J. T. (2013) Metal–Organic Framework Thin Films Composed of Free-Standing Acicular Nanorods Exhibiting Reversible Electrochromism. *Chem. Mater.* 25, 5012–5017. e) D'Alessandro, D. (2016) Exploiting redox activity in metal–organic frameworks: concepts, trends and perspectives *Chem. Commun.* in press (DOI: 10.1039/C6CC00805D).

<sup>3</sup> a) Stavila, V.; Talin, A. A.; Allendorf, M. D. (2014) MOF-Based Electronic and Opto-Electronic Devices. *Chem. Soc. Rev.* 43, 5994. b) Kobayashi, Y.; Jacobs, B.; Allendorf, M. D.; Long, J. R. (2010) Conductivity, Doping, and Redox Chemistry of a Microporous Dithiolene-Based Metal–Organic Framework. *Chem. Mater.* 22, 4120–4122. c) Sun, L.; Campbell, M. G.; Dincă, M. (2016) Electrically Conductive Porous Metal–Organic Frameworks. *Angew. Chem. Int. Ed.* 55, 2 –16. d) Jeon, I.-R.; Sun, L.; Negru, B.; Van Duyne, R. P.; Dincă, M.; Harris, T. D. (2016) Solid-State Redox Switching of Magnetic Exchange and Electronic Conductivity in a Benzoquinoid-Bridged Mn<sup>II</sup> Chain Compound. *J. Am. Chem. Soc.* 138, in press (DOI: 10.1021/jacs.6b02485).

<sup>4</sup> Shekhah, O.; Liu, J.; Fischer, R. A.; Wöll, C. (2011) MOF Thin Films: Existing and Future Applications. *Chem. Soc. Rev.* 40(2), 1081–27.

<sup>5</sup> Bradshaw, D.; Garai, A.; Huo, J. (2012) Metal–organic Framework Growth at Functional Interfaces: Thin Films and Composites for Diverse Applications. *Chem. Soc. Rev.* 41(6), 2344–2381.

<sup>6</sup> Allendorf, M. D.; Schwartzberg, A.; Stavila, V.; Talin, A. A. (2011) A Roadmap to Implementing Metal–Organic Frameworks in Electronic Devices: Challenges and Critical Directions. *Chem. Eur. J.* 17(41), 11372–11388.

<sup>7</sup> a) Deng, H.; Grunder, S.; Cordova, K. E.; Valente, C.; Furukawa, H.; Hmadeh, M.; Gandara, F.; Whalley, A. C.; Liu, Z.; Asahina, S.; Kazumori, H.; O’Keeffe, M.; Terasaki, O.; Stoddart, J. F.; Yaghi, O. M. (2012) Large-Pore Apertures in a Series of Metal–Organic Frameworks. *Science* 336, 1018. b) Kapelewski, M. T.; Geier, S. J.; Hudson, M. R.; Stück, D.; Mason, J. A.; Nelson, J. N.; Xiao, D. J.; Hulvey, Z.; Gilmour, E.;



---

FitzGerald, S. A.; Head-Gordon, M.; Brown, C. M.; Long, J. R. (2014)  $M_2(m\text{-dobdc})$  ( $M = \text{Mg, Mn, Fe, Co, Ni}$ ) Metal–Organic Frameworks Exhibiting Increased Charge Density and Enhanced  $H_2$  Binding at the Open Metal Sites. *J. Am. Chem. Soc.* 136(34), 12119–12129. c) Cozzolino, A. F.; Brozek, C. K.; Palmer, R. D.; Yano, J.; Li, M.; Dincă, M. (2014) Ligand Redox Non-innocence in the Stoichiometric Oxidation of Mn 2(2,5-dioxidoterephthalate) (Mn-MOF-74). *J. Am. Chem. Soc.* 136(9), 3334–3337. d) Aubrey, M. L.; Long, J. R. (2015) A Dual–Ion Battery Cathode via Oxidative Insertion of Anions in a Metal–Organic Framework. *J. Am. Chem. Soc.* 137, 13594–13602.

<sup>8</sup> a) Suraru, S.-L.; Würthner, F. (2014) Strategies For the Synthesis of Functional Naphthalene Diimides. *Angew. Chem., Int. Ed.* 53(29), 7428–7448. b) Bhosale, S. V.; Jani, C. H.; Langford, S. (2008) Chemistry of Naphthalene Diimides. *J. Chem. Soc. Rev.* 37(2), 331–342. c) Guha, S.; Goodson, F. S.; Corson, L. J.; Saha, S. (2012) Boundaries of Anion/Naphthalenediimide Interactions: From Anion– $\pi$  Interactions to Anion-Induced Charge-Transfer and Electron-Transfer Phenomena. *J. Am. Chem. Soc.* 134(33), 13679–13691.

<sup>9</sup> a) Takashima, Y.; Martinez, V. M.; Furukawa, S.; Kondo, M.; Shimomura, S.; Uehara, H.; Nakahama, M.; Sugimoto, K.; Kitagawa, S. (2011) Molecular Decoding Using Luminescence From an Entangled Porous Framework. *Nat. Comms.* 2, 168. b) Mallick, A.; Garai, B.; Addicoat, M. A.; Petkov, P. S.; Heine, T.; Banerjee, R. (2015) Solid State Organic Amine Detection in a Photochromic Porous Metal Organic Framework. *Chem. Sci.* 6, 1420–1425.

<sup>10</sup> The structure can be simulated equally well in space groups  $R3$  and  $R\bar{3}$ .

<sup>11</sup> Monk, P. M. S.; Mortimer, R. J.; Rosseinsky, D. R. (2007) *Electrochromism and Electrochromic Devices*. (New York: Cambridge University Press).

<sup>12</sup> a) Beaujuge, P. M.; Ellinger, S.; Reynolds, J. R. (2008) The Donor-Acceptor Approach Allows a Black-to-Transmissive Switching Polymeric Electrochrome. *Nat. Mater.* 7, 795. b) Hsu, P. -C.; Wang, S.; Narasimhan, V. K.; Kong, D.; Lee, H. R.; Cui, Y. (2013) Performance enhancement of metal nanowire transparent conducting electrodes by mesoscale metal wires. *Nat. Commun.* 4, 2522.

## Appendix A. Structural information: CIF files for simulated structures.

### a. Mg-NDISA CIF File

data\_Structure\after\refinement

\_audit\_creation\_date 2016-01-08  
\_audit\_creation\_method 'Materials Studio'  
\_symmetry\_space\_group\_name\_H-M 'R3'  
\_symmetry\_Int\_Tables\_number 146  
\_symmetry\_cell\_setting trigonal

loop\_

\_symmetry\_equiv\_pos\_as\_xyz

x,y,z

-y,x-y,z

-x+y,-x,z

x+2/3,y+1/3,z+1/3

-y+2/3,x-y+1/3,z+1/3

-x+y+2/3,-x+1/3,z+1/3

x+1/3,y+2/3,z+2/3

-y+1/3,x-y+2/3,z+2/3

-x+y+1/3,-x+2/3,z+2/3

\_cell\_length\_a 59.1755  
\_cell\_length\_b 59.1755  
\_cell\_length\_c 7.4668  
\_cell\_angle\_alpha 90.0000  
\_cell\_angle\_beta 90.0000  
\_cell\_angle\_gamma 120.0000

loop\_

\_atom\_site\_label

\_atom\_site\_type\_symbol

\_atom\_site\_fract\_x

\_atom\_site\_fract\_y

\_atom\_site\_fract\_z

\_atom\_site\_U\_iso\_or\_equiv

\_atom\_site\_adp\_type

\_atom\_site\_occupancy

H1	H	0.77873	0.12071	-0.54481	0.00000	Uiso	1.00
H2	H	0.74222	0.08504	-0.76591	0.00000	Uiso	1.00
H3	H	0.74386	0.06430	-0.04858	0.00000	Uiso	1.00
H4	H	0.92318	0.26644	0.38404	0.00000	Uiso	1.00
H5	H	0.92550	0.24805	1.10507	0.00000	Uiso	1.00
H6	H	0.88912	0.21177	0.88743	0.00000	Uiso	1.00
C7	C	0.74245	0.08054	-0.60436	0.05000	Uiso	1.00
C8	C	0.76255	0.10025	-0.48226	0.05000	Uiso	1.00
C9	C	0.76289	0.09496	-0.28253	0.05000	Uiso	1.00
C10	C	0.74335	0.06932	-0.20872	0.05000	Uiso	1.00
C11	C	0.94445	0.28294	0.66388	0.05000	Uiso	1.00
C12	C	0.94532	0.27791	0.86811	0.05000	Uiso	1.00
C13	C	0.72206	0.05476	-0.53153	0.05000	Uiso	1.00
C14	C	0.72287	0.04934	-0.32804	0.05000	Uiso	1.00
C15	C	0.92414	0.26250	0.54581	0.05000	Uiso	1.00
C16	C	0.90479	0.23707	0.62313	0.05000	Uiso	1.00
C17	C	0.90514	0.23213	0.82263	0.05000	Uiso	1.00
C18	C	0.92515	0.25219	0.94297	0.05000	Uiso	1.00
C19	C	0.70469	0.02507	-0.22951	0.05000	Uiso	1.00
O20	O	0.68606	0.00587	-0.33170	0.05000	Uiso	1.00
O21	O	0.70867	0.02055	-0.05124	0.05000	Uiso	1.00
O22	O	0.70193	0.03492	-0.65433	0.00000	Uiso	1.00

O23	O	0.96722	0.29997	1.00046	0.00000	Uiso	1.00
C24	C	0.96403	0.30947	0.54680	0.00000	Uiso	1.00
O25	O	0.96024	0.31092	0.34740	0.00000	Uiso	1.00
O26	O	0.98510	0.33146	0.64280	0.00000	Uiso	1.00
Mg27	Mg	0.33167	0.34833	-0.18167	0.04000	Uiso	1.00
Mg28	Mg	0.68067	0.68233	0.81633	0.05334	Uiso	1.00
O29	O	0.81417	0.10089	-0.20809	0.00000	Uiso	1.00
C30	C	0.85487	0.13843	0.03760	0.00000	Uiso	1.00
C31	C	0.80951	0.11782	-0.12699	0.00000	Uiso	1.00
C32	C	0.82950	0.13754	0.00321	0.00000	Uiso	1.00
C33	C	0.87443	0.15799	0.16765	0.00000	Uiso	1.00
H34	H	0.85963	0.12398	-0.03619	0.00000	Uiso	1.00
N35	N	0.78437	0.11697	-0.15831	0.00000	Uiso	1.00
C36	C	0.77904	0.13599	-0.06136	0.00000	Uiso	1.00
C37	C	0.82395	0.15656	0.10194	0.00000	Uiso	1.00
H38	H	0.89377	0.15812	0.19052	0.00000	Uiso	1.00
C39	C	0.86913	0.17718	0.26664	0.00000	Uiso	1.00
O40	O	0.91035	0.19706	0.42930	0.00000	Uiso	1.00
C41	C	0.79866	0.15583	0.06937	0.00000	Uiso	1.00
C42	C	0.84381	0.17642	0.23403	0.00000	Uiso	1.00
C43	C	0.88871	0.19704	0.39796	0.00000	Uiso	1.00
O44	O	0.75744	0.13606	-0.09278	0.00000	Uiso	1.00
C45	C	0.79336	0.17504	0.16810	0.00000	Uiso	1.00
C46	C	0.83824	0.19541	0.33274	0.00000	Uiso	1.00
N47	N	0.88325	0.21591	0.49555	0.00000	Uiso	1.00
C48	C	0.81288	0.19456	0.29817	0.00000	Uiso	1.00
C49	C	0.85812	0.21506	0.46345	0.00000	Uiso	1.00
H50	H	0.77403	0.17493	0.14518	0.00000	Uiso	1.00

O51 O 0.85340 0.23196 0.54437 0.00000 Uiso 1.00

H52 H 0.80812 0.20901 0.37194 0.00000 Uiso 1.00

loop\_

\_geom\_bond\_atom\_site\_label\_1

\_geom\_bond\_atom\_site\_label\_2

\_geom\_bond\_distance

\_geom\_bond\_site\_symmetry\_2

\_ccdc\_geom\_bond\_type

H1 C8 1.201 . S

H2 C7 1.237 . S

H3 C10 1.236 . S

H4 C15 1.237 . S

H5 C18 1.237 . S

H6 C17 1.201 . S

C7 C8 1.490 . A

C7 C13 1.496 . A

C8 C9 1.526 . A

C9 C10 1.479 . A

C9 N35 1.586 . S

C10 C14 1.492 . A

C11 C12 1.560 . A

C11 C15 1.494 . A

C11 C24 1.659 . S

C12 C18 1.496 . A

C12 O23 1.634 . S

C13 C14 1.559 . A

C13 O22 1.497 . S

C14 C19 1.489 . S

C15	C16	1.478	.	A
C16	C17	1.520	.	A
C16	N47	1.582	.	S
C17	C18	1.488	.	A
C19	O20	1.355	.	A
C19	O21	1.401	.	A
C24	O25	1.514	.	A
C24	O26	1.463	.	A
O29	C31	1.313	.	D
C30	C32	1.498	.	D
C30	C33	1.511	.	S
C30	H34	1.164	.	S
C31	C32	1.525	.	S
C31	N35	1.482	.	S
C32	C37	1.513	.	S
C33	H38	1.153	.	S
C33	C39	1.513	.	D
N35	C36	1.498	.	S
C36	C41	1.522	.	S
C36	O44	1.302	.	D
C37	C41	1.495	.	S
C37	C42	1.534	.	D
C39	C42	1.496	.	S
C39	C43	1.524	.	S
O40	C43	1.301	.	D
C41	C45	1.513	.	D
C42	C46	1.512	.	S
C43	N47	1.498	.	S

C45	C48	1.509	.	S
C45	H50	1.153	.	S
C46	C48	1.499	.	D
C46	C49	1.523	.	S
N47	C49	1.482	.	S
C48	H52	1.164	.	S
C49	O51	1.312	.	D

## b. Ni-NDISA CIF File

data\_Structure\after\refinement-Ni

```
_audit_creation_date      2016-05-26
_audit_creation_method    'Materials Studio'
_symmetry_space_group_name_H-M  'R3'
_symmetry_Int_Tables_number  146
_symmetry_cell_setting     trigonal
loop_
_symmetry_equiv_pos_as_xyz
  x,y,z
  -y,x-y,z
  -x+y,-x,z
  x+2/3,y+1/3,z+1/3
  -y+2/3,x-y+1/3,z+1/3
  -x+y+2/3,-x+1/3,z+1/3
  x+1/3,y+2/3,z+2/3
  -y+1/3,x-y+2/3,z+2/3
  -x+y+1/3,-x+2/3,z+2/3
_cell_length_a           59.7979
_cell_length_b           59.7979
_cell_length_c           7.3994
_cell_angle_alpha        90.0000
_cell_angle_beta         90.0000
_cell_angle_gamma        120.0000
loop_
_atom_site_label
_atom_site_type_symbol
_atom_site_fract_x
```



\_atom\_site\_fract\_y

\_atom\_site\_fract\_z

\_atom\_site\_U\_iso\_or\_equiv

\_atom\_site\_adp\_type

\_atom\_site\_occupancy

H1	H	0.77873	0.12071	-0.54481	0.00000	Uiso	1.00
H2	H	0.74222	0.08504	-0.76591	0.00000	Uiso	1.00
H3	H	0.74386	0.06430	-0.04858	0.00000	Uiso	1.00
H4	H	0.92318	0.26644	0.38404	0.00000	Uiso	1.00
H5	H	0.92550	0.24805	1.10507	0.00000	Uiso	1.00
H6	H	0.88912	0.21177	0.88743	0.00000	Uiso	1.00
C7	C	0.74245	0.08054	-0.60436	0.05000	Uiso	1.00
C8	C	0.76255	0.10025	-0.48226	0.05000	Uiso	1.00
C9	C	0.76289	0.09496	-0.28253	0.05000	Uiso	1.00
C10	C	0.74335	0.06932	-0.20872	0.05000	Uiso	1.00
C11	C	0.94445	0.28294	0.66388	0.05000	Uiso	1.00
C12	C	0.94532	0.27791	0.86811	0.05000	Uiso	1.00
C13	C	0.72206	0.05476	-0.53153	0.05000	Uiso	1.00
C14	C	0.72287	0.04934	-0.32804	0.05000	Uiso	1.00
C15	C	0.92414	0.26250	0.54581	0.05000	Uiso	1.00
C16	C	0.90479	0.23707	0.62313	0.05000	Uiso	1.00
C17	C	0.90514	0.23213	0.82263	0.05000	Uiso	1.00
C18	C	0.92515	0.25219	0.94297	0.05000	Uiso	1.00
C19	C	0.70469	0.02507	-0.22951	0.05000	Uiso	1.00
O20	O	0.68606	0.00587	-0.33170	0.05000	Uiso	1.00
O21	O	0.70867	0.02055	-0.05124	0.05000	Uiso	1.00
O22	O	0.70193	0.03492	-0.65433	0.00000	Uiso	1.00
O23	O	0.96722	0.29997	1.00046	0.00000	Uiso	1.00

C24	C	0.96403	0.30947	0.54680	0.00000	Uiso	1.00
O25	O	0.96024	0.31092	0.34740	0.00000	Uiso	1.00
O26	O	0.98510	0.33146	0.64280	0.00000	Uiso	1.00
Ni27	Ni	0.33167	0.34833	-0.18167	0.04000	Uiso	1.00
Ni28	Ni	0.68067	0.68233	0.81633	0.05334	Uiso	1.00
O29	O	0.81417	0.10089	-0.20809	0.00000	Uiso	1.00
C30	C	0.85487	0.13843	0.03760	0.00000	Uiso	1.00
C31	C	0.80951	0.11782	-0.12699	0.00000	Uiso	1.00
C32	C	0.82950	0.13754	0.00321	0.00000	Uiso	1.00
C33	C	0.87443	0.15799	0.16765	0.00000	Uiso	1.00
H34	H	0.85963	0.12398	-0.03619	0.00000	Uiso	1.00
N35	N	0.78437	0.11697	-0.15831	0.00000	Uiso	1.00
C36	C	0.77904	0.13599	-0.06136	0.00000	Uiso	1.00
C37	C	0.82395	0.15656	0.10194	0.00000	Uiso	1.00
H38	H	0.89377	0.15812	0.19052	0.00000	Uiso	1.00
C39	C	0.86913	0.17718	0.26664	0.00000	Uiso	1.00
O40	O	0.91035	0.19706	0.42930	0.00000	Uiso	1.00
C41	C	0.79866	0.15583	0.06937	0.00000	Uiso	1.00
C42	C	0.84381	0.17642	0.23403	0.00000	Uiso	1.00
C43	C	0.88871	0.19704	0.39796	0.00000	Uiso	1.00
O44	O	0.75744	0.13606	-0.09278	0.00000	Uiso	1.00
C45	C	0.79336	0.17504	0.16810	0.00000	Uiso	1.00
C46	C	0.83824	0.19541	0.33274	0.00000	Uiso	1.00
N47	N	0.88325	0.21591	0.49555	0.00000	Uiso	1.00
C48	C	0.81288	0.19456	0.29817	0.00000	Uiso	1.00
C49	C	0.85812	0.21506	0.46345	0.00000	Uiso	1.00
H50	H	0.77403	0.17493	0.14518	0.00000	Uiso	1.00
O51	O	0.85340	0.23196	0.54437	0.00000	Uiso	1.00

H52 H 0.80812 0.20901 0.37194 0.00000 Uiso 1.00

loop\_

\_geom\_bond\_atom\_site\_label\_1

\_geom\_bond\_atom\_site\_label\_2

\_geom\_bond\_distance

\_geom\_bond\_site\_symmetry\_2

\_ccdc\_geom\_bond\_type

H1	C8	1.210	.	S
H2	C7	1.227	.	S
H3	C10	1.226	.	S
H4	C15	1.227	.	S
H5	C18	1.227	.	S
H6	C17	1.210	.	S
C7	C8	1.494	.	A
C7	C13	1.508	.	A
C8	C9	1.514	.	A
C9	C10	1.491	.	A
C9	N35	1.593	.	S
C10	C14	1.498	.	A
C11	C12	1.547	.	A
C11	C15	1.499	.	A
C11	C24	1.668	.	S
C12	C18	1.507	.	A
C12	O23	1.639	.	S
C13	C14	1.546	.	A
C13	O22	1.501	.	S
C14	C19	1.497	.	S
C15	C16	1.490	.	A

C16	C17	1.508	.	A
C16	N47	1.588	.	S
C17	C18	1.493	.	A
C19	O20	1.361	.	A
C19	O21	1.391	.	A
C24	O25	1.502	.	A
C24	O26	1.471	.	A
O29	C31	1.321	.	D
C30	C32	1.513	.	D
C30	C33	1.515	.	S
C30	H34	1.171	.	S
C31	C32	1.529	.	S
C31	N35	1.497	.	S
C32	C37	1.521	.	S
C33	H38	1.165	.	S
C33	C39	1.522	.	D
N35	C36	1.507	.	S
C36	C41	1.526	.	S
C36	O44	1.314	.	D
C37	C41	1.510	.	S
C37	C42	1.538	.	D
C39	C42	1.511	.	S
C39	C43	1.528	.	S
O40	C43	1.314	.	D
C41	C45	1.522	.	D
C42	C46	1.521	.	S
C43	N47	1.507	.	S
C45	C48	1.513	.	S

C45	H50	1.165	.	S
C46	C48	1.513	.	D
C46	C49	1.527	.	S
N47	C49	1.497	.	S
C48	H52	1.171	.	S
C49	O51	1.321	.	D

# KHALID A. AL KAABI

607.379.4112

kalkaabi@mit.edu

kaa63@cornell.edu

---

## EDUCATION

### Massachusetts Institute of Technology

Master of Science in Chemistry (Advisor: Mircea Dincă)

Cambridge, MA

Sep. 2014 – Sep. 2016

Thesis Title: “Transparent-to-Dark Electrochromic Behavior in Naphthalene-Diimide-Based Mesoporous MOF-74 Analogs”

Full Scholarship from Saudi Aramco’s Research and Development Center

### Cornell University

Bachelor of Science in Chemical Engineering

Ithaca, NY

Aug. 2009 – May 2014

CGPA: 3.87 (*magna cum laude*)

Dean’s List (Spring 2010, Fall 2012, Spring 2012, and Spring 2013)

Full Scholarship from Saudi Aramco

## RESEARCH EXPERIENCE

### Massachusetts Institute of Technology, Department of Chemistry

Research Assistant with Prof. Mircea Dincă

Cambridge, MA

Sep. 2014 – Sep. 2016

- Designed and conducted experimental identification and characterization of electrochromic metal-organic frameworks.
- One publication that appeared on the cover of the new journal *Chem* (Cell Press), and was highlighted in MIT News.
- Presented the results in ACS conference (San Diego, 2016) and IdeaStream (MIT Deshpande center, 2016).

### Cornell University, Department of Chemistry and Chemical Biology

Research Assistant with Prof. Roald Hoffmann

Ithaca, NY

Nov. 2011 – May 2014

- Conducted theoretical analysis of silicon monoxide at 1 atm and elevated pressures.
- Conducted theoretical analysis of ionic boron-nitrogen substituted benzene analogues.
- Two publications in the *Journal of American Chemical Society*.

### Cornell University, Department of Chemistry and Chemical Biology

Research Assistant with Prof. William Dichtel

Ithaca, NY

Oct. 2013 – May 2014

- Conducted experimental identification and characterization of unknown side-products of acid catalyzed benzannulation reaction of o-alkynyl(oxo)benzenes with alkynes.

## PEER-REVIEWED PUBLICATIONS

**AlKaabi, K.**; Wade, C. R., Dincă, M. “Transparent-to-Dark Electrochromic Behavior in Naphthalene-Diimide-Based Mesoporous MOF-74 Analogs” *Chem*, **2016**, 1, pp 264 – 272.

**AlKaabi, K.**; Dasari, P.L.V.K.; Hoffmann, R. “Ionic N–B–N- and B–N–B-Substituted Benzene Analogues: A Theoretical Analysis” *J. Am. Chem. Soc.*, **2012**, 134 (29), pp 12252 – 12258.

**AlKaabi, K.**; Dasari, P.L.V.K.; Kroll, P.; Ashcroft, N. W.; Hoffmann, R. “Silicon Monoxide, at 1 atm and Elevated Pressures: Crystalline or Amorphous?” *J. Am. Chem. Soc.* **2014**, 136 (9), pp 3410 – 3423.

## **TECHNICAL SKILLS**

- Routinely Utilized Scanning Electron Microscopy (SEM), Powder X-ray diffraction, NMR, UV-Vis, gas sorption, and electrochemical techniques.
- Familiar with organic synthesis, Schlenck techniques, and glovebox techniques.
- Materials Studio and Gaussian electronic structure software.
- Vienna Ab initio simulation package (VASP).
- Linux, Mathematica, Origin, Adobe Illustrator.
- Proficient in Excel, Word, PowerPoint.

## **INTERESTS**

Playing the Oud (lute), Soccer, horseback riding, squash, and traveling.